Dynamic response reconstruction of an FRC blade with embedded piezoelectric sensors

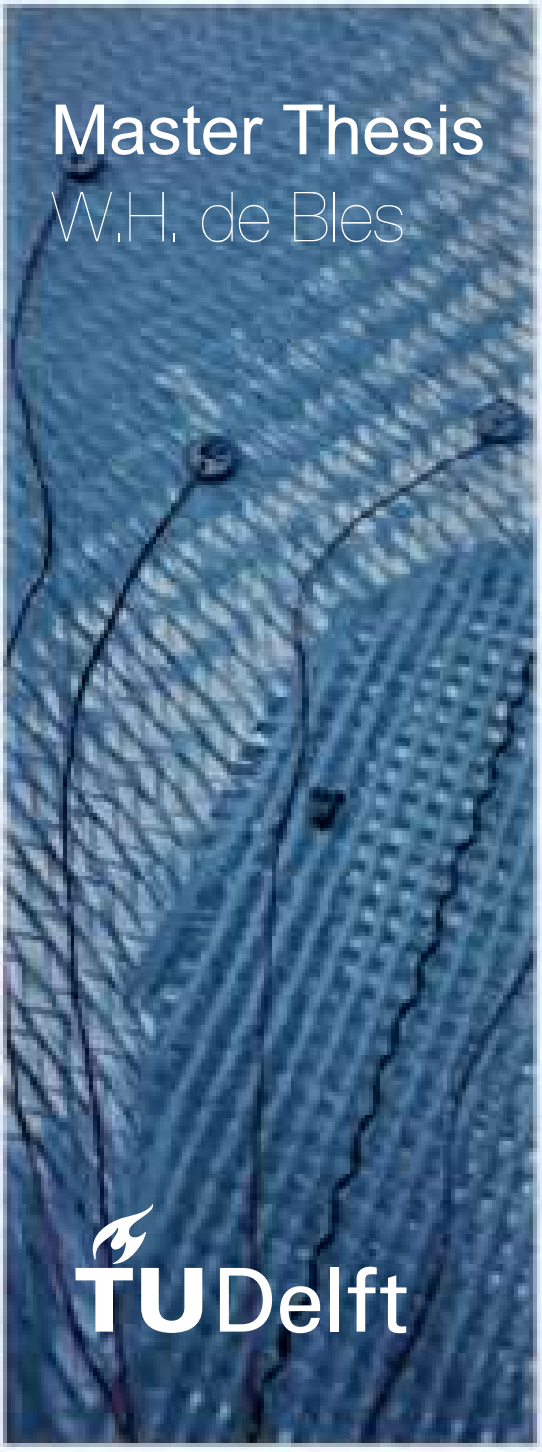

Delft University of Technology

Dynamic response reconstruction of an FRC blade with embedded piezoelectric sensors

by

W.H. de Bles

to obtain the degree of Master of Science
at the Delft University of Technology,
to be defended publicly on Tuesday April 5, 2022 at 10:45 AM.

Student number:	4420055	
Report number:	MT.21/22.026.M	
Project duration:	1st March 2021 - 5th April 2022	
Thesis committee:	Prof. Dr. MSc. T.J.C. van Terwisga	TU Delft, chair
	Dr. MSc. L. Pahlavan,	TU Delft, supervisor
	MSc. A.J. Huijer,	TU Delft, daily supervisor
	Prof. Dr. MSc. C. Kassapoglou	TU Delft
	Dr. MSc. A. Grammatikopoulos	TU Delft

An electronic version of this thesis is available at `http://repository.tudelft.nl/`.

TU Delft

Abstract

Fiber-reinforced composite (FRC) marine propellers potentially outperform metallic propellers in terms of efficiency and underwater radiated noise (URN) by hydro-elastic tailoring of the blades. Several methods can assess the extent of these potentials. Research shows that embedded sensing methods can be used in dynamic measurements of composites. This thesis studies a full-scale application of a network of embedded piezoelectric sensors in an FRC marine propeller blade. The study prefers using piezoelectric sensors because of their ability to operate in a relatively wide frequency range.

The focus of the thesis starts with designing the full-scale network of embedded piezoelectric sensors. Since no literature includes this application on FRC blades, this study holds a pioneering role in embedding piezoelectric sensors in an FRC marine propeller blade. Detailed analysis of material dimensions - including sensors, wiring, and fiber plies - leads to a successful sensor network design. Considerations regarding the location of 24 sensors included both the in-plane and the in-depth position within the FRC laminate.

Fabrication of an FRC blade has been done using a resin transfer moulding (RTM) process. For the first time, an FRC marine propeller blade is embedded with piezoelectric sensors. Demoulding of the blade caused damage to some of the sensor wires. An amount of 54% of the embedded sensors survived the process with full connectivity.

The performance of the intact sensors after fabrication is assessed. These sensors are exposed to free vibration tests of the FRC blade. An excitation is imposed on the blade with an impact hammer. A data acquisition (DAQ) system is used to capture the responses of the embedded piezo-sensors. The frequency response functions (FRFs) of multiple locations on the blade are computed. These FRFs provide more insight into the dynamic behavior of the blade. A frequency range of 1-1000Hz is used in the modal analysis. The first five natural frequencies are found between 240Hz and 840Hz. Natural frequencies measured by the embedded piezo-sensors and surface-mounted strain gauges differ up until 25% from natural frequencies computed by a finite element model (FEM) of the blade.

The mode shape of the blade at the natural frequencies is computed for by the FEM and embedded piezo-sensors. Some difference in mode shapes is demonstrated between measurements computed by FEM and those measured by the embedded piezo-sensors and surface-mounted strain gauges. The piezo-sensors and strain gauges are in agreement regarding the measured natural frequencies. Therefore, it is expected that discrepancies exist between the physical blade and FEM.

Several points for improvement of the results have been found. The study provides the first-time feasibility of dynamic measurements from embedded piezo-sensors in an FRC marine propeller blade. Additionally, a framework for reconstructing the full-field vibration response is provided, which can provide more accurate results when the agreement between piezo-sensor and FEM measurements has improved.

Preface

This thesis study is part of ECoProp, a multi-company project focussed on realizing a self-monitoring composite propeller. Delft University of Technology is part of this project. The study is proposed by Dr. L. Pahlavan, Assistant Professor Ship and Offshore Structures of Maritime and Transport Technology Department of the Delft University of Technology.

The research is performed as Master Thesis Project at the department Ship and Offshore Structures, Faculty 3mE, Delft University of Technology. My gratitude goes to Pooria Pahlavan for suggesting this thesis subject and giving me the opportunity to be part of ECoProp. Also, Arno Huijer deserves both my appreciation and recognition for his daily efforts in supervising my work. In addition, I would like to thank the graduates, who are also under Pooria his supervision, for the biweekly progress meetings and, in particular, Filippo Riccioli for planning extra meetings to have profound discussions.

Furthermore, I am thankful to Xiaobo Zhang and Pieter Maljaars for providing the finite element model and the program's guidelines. Additionally, the contact with Pieter Maljaars supplied crucial components for the experiments.

The suggestions by Christos Kassapoglou regarding the interpretation of theory and practical parts in the blade fabrication are deeply appreciated. Also, the advice for having a critical view on experimental results by Apostolos Grammatikopoulos proved its value during the final part of writing this thesis.
My gratitude goes to the user committee members of ECoProp, the employees of the towing tank, and the employees of Jules Dock Composites for their support and contribution to this project.

Finally, I am thankful for the support my family, friends, and girlfriend gave me the past year. Their love and encouragement helped me relax after stressful times.

W.H. de Bles
Delft, March 2022

Contents

Nomenclature

Abbreviations

Abbreviation	Definition
CFRP	Carbon Fiber Reinforced Polymer
CLT	Classical Laminate Theory
CT	Computed Tomography
DAQ	Data Acquisition
DOF	Degree Of Freedom
DIC	Digital Image Correlation
ECoProp	Ecological Composite Propeller
FBG	Fiber Bragg Grating
FE	Finite Element
FEM	Finite Element Method / Finite Element Model
FFT	Fast Fourier Transform
FRC	Fiber Reinforced Composite
FRF	Frequency Response Function
FRP	Fiber Reinforced Polymer
GF	Gauge Factor
GFRP	Glass Fiber Reinforced Polymer
MAC	Modal Assurance Criterion
NAB	Nickel Aluminium Bronze
NI	National Instruments
OD	Outer Diameter
PPE	Personal Protective Equipment
PZT	Piezoelectric Lead Zirconate Titanate
RTM	Resin Transfer Moulding
SHM	Structural Health Monitoring
SMA	Sub-Miniature Version A
SMART	Stanford MultiActuatorReceiver Transduction
TH	Thickness
UD	Unidirectional
URN	Underwater Radiated Noise
USB	Universal Serial Bus
VSRTM	Vacuum-supported Resin Transfer Moulding

Symbols

Symbol	Definition	Unit
A	Initial deflection	[m]
A_p	Area of piezoelectric sensor	[m^2]
B	Initial velocity	[ms^{-1}]]
b	Directional vector of piezoelectric effect	[-]
C_sv	Strain-voltage relation strain gauge	[mV^{-1}]
C_{elec}	Electrical capacitance	[F]
C_m	Capacitance of measurement system	[F]
C_s	Capacitance of sensor	[F]
c^E	Mechanical stiffness	[Nm^{-1}]
d	Distance between PZT sensing plates	[m]
D_m	Electric flux density	[Cm^{-2}]
d^θ_{ijn}	Piezoelectric strain constant	[mV^{-1}]
d^θ_{mkl}	Piezoelectric stress constant	[CN^{-}]
d^σ	Piezoelectric strain constant at constant stress	[CN^{-}]
e_{ijn}	Electro-mechanical coupling coefficient	[-]
e_{mkl}	Electro-mechanical coupling coefficient	[-]
E_m	Electric field intensity	[Vm^{-1}]
F_s	Current source term (e.g. socket)	[Cs^{-1}]
F_θ	Current source term (e.g. DAQ)	[Cs^{-1}]
G_x	Surface-mounted strain gauge	[-]
H	Electro-mechanical matrix	[Vm m^{-1}]
H_{full}	Full electro-mechanical matrix	[Vm m^{-1}]
h_n	Electro-mechanical term	[Vm·m^{-1}]
I	Current	[A]
I_{loc}	Impact location	[-]
I_m	Current of measurement components	[A]
I_s	Current of sensors	[A]
L	Length of strain gauge [m]	
n_m	Number of modes	[-]
n_s	Number of sensors	[-]
n_{sdof}	Number of degrees of freedom	[-]
n_t	Number of time-steps	[-]
P	Pressure	[hPa]
Q	Heat energy	[J]
Q_{heat}	Heat energy	[J]
R_1	First impedance of strain gauge	[Ω]
R_2	Second impedance of strain gauge	[Ω]
R_m	Impedance of measurement system	[Ω]
R_s	Impedance of strain gauge amplifier	[Ω]
R_v	Variable impedance on substitute specimen	[Ω]
$s^{E,\theta}_{ijkl}$	Elastic compliance constant	[m^2N^{-1}]
$\mathfrak{s}$	Entropy	[JK^{-1}]
S_{ij}	Mechanical strain	[-]
T	Time component of vibration	[s]
T_{ij}	Mechanical stress	[Nm^{-2}]
$Tmould$	Temperature of mould surface	[deg]
T_{pcv}	Principal coordinate vector	[-]
T_{resin}	Temperature of resin mixture bucket	[deg]
$T_{tube,in}$	Temperature of resin import tube	[deg]
$T_{tube,out}$	Temperature of resin export tube	[deg]
t	Time	[s]
t_p	Thickness of piezoelectric sensor	[m]

Symbol	Definition	Unit
U	Internal energy	[J]
U_1	Measured voltage of strain gauge	[V]
U_2	Measured voltage of amplifier	[V]
V	Voltage	[V]
V	Full voltage vector	[V]
W	Work	[J]
W_{mech}	Work as electric energy	[J]
W_{elec}	Work as mechanic energy	[J]
z	Embedding depth	[m]
α_{ij}^{E}	Thermal expansion coefficient	[K^{-1}]
ε_0	Initial strain on strain gauge	[$m \cdot m^{-1}$]
$\varepsilon_{mn}^{T,\theta}$	Electric permittivity	[$AsV^{-1}m^{-1}$]
$\varepsilon^{\varepsilon}$	Electric permittivity at constant strain	[$AsV^{-1}m^{-1}$]
ε^{σ}	Electric permittivity at constant stress	[$AsV^{-1}m^{-1}$]
ε_{pv}	Permitivity in vacuum	[$AsV^{-1}m^{-1}$]
θ	Temperature	[kg m^{-3}]
ρ_m^T	Pyroelectric coefficient	[$Cm^{-2}K^{-1}$]
Φ	Space component of vibration	[-]
$\vec{\phi}$	Modal vector	[-]
ϕ_{elec}	Polarization indicator	[-]
φ	Piezoelectric material indicator	[-]
φ_{sg}	Modal strain vector of strain gauges	[-]
φ_{fem}	Modal strain vector of FEM	[-]
Ψ	Main modal strain matrix	[$m \cdot m^{-1}$]
Ψ_{full}	Full modal strain matrix	[$m \cdot m^{-1}$]
Ψ_r	Reduced modal strain matrix	[$m \cdot m^{-1}$]
$\psi_{n,m}$	Strain mode shape vector	[$m \cdot m^{-1}$]
ω	Angular velocity	[$rads^{-1}$]
Ω_p	Volume of piezoelectric material	[m^3]

List of Figures

List of Tables

1 Introduction

1.1. Background

Conventional marine propellers are produced from alloys, such as nickel, aluminum, and bronze (NAB) material. However, composite materials are advancing, with research showing potential in applications where composite marine propellers outperform those made from conventional materials. The two main advantages are reducing underwater radiated noise (URN) and electro-mechanical signature.

In composite design, shape adaptive marine propeller blades can be achieved using the unique composite properties. Due to the high tensile strength of certain FRCs, the blade is allowed to be thinner and thus more flexible compared to materials with lower strength. Hydro-elastic tailoring of the blade can achieve increased efficiency in multiple loading conditions [1]. Improved off-design conditions reduce initiation of cavitation[1]; the main contributor to URN. Hence, the flexibility due to high strength potentially leads to increased efficiency and decreased URN.

To realize these potential advantages, the design of composite marine propellers must be assessed and improved. Maljaars [2] executed full-scale composite propeller tests in structural response was measured with digital image correlation (DIC). This method showed to be too challenging in open-water application due to reduced visibility. Other methods exist for which visibility is no disadvantage, such as sensing applications used within composites. The layered structure of composites grants the ability to embed sensors in a marine propeller. Fiber-Bragg Gratings (FBG) offer such a solution in embedded measurements of strain and vibrations in a marine propeller blade [3][4][5]. FBG is a thin fiber wavered in-between fiber layers, which can provide limited influence on the structural integrity [6]. However, their small diameter makes FBG prone to fracture and vigilant production is required. In addition to dynamic measurements, it is possible to do static measurements on a marine propeller blade with an FBG network [7][2].

In order to assess the quality of structural response measurements of embedded sensing methods such as FBG, their output can be compared with surface-mounted strain gauges [8][9]. Surface-mounted strain gauges are no independent solution for this study because of the operational environment of marine propeller blades. Also, both FBG and strain gauges have a limited capability of measuring the higher frequencies. Piezoelectric sensors appear to be applicable in a wider frequency range. This ability makes it possible to measure both vibrations within the low-frequency region and acoustic emissions in the higher frequency region. Capturing both regions in a single method is preferred. The current research is focused on the application of a composite marine propeller blade with an embedded piezoelectric sensor. The sensors are used in the low-frequency measurements concerning the

[1] Cavitation is the phenomenon in which the static local pressure becomes lower than the vapor pressure of the liquid. Water then evaporates at a temperature lower than the usual 100° C. The air bubbles implode in an environment with higher pressures, which causes noise and can damage surroundings.

[2] This is convenient for the theory that the wake field can become uniform and deformation rate in a rotation becomes zero. In that case, a static situation is assumed where an FBG network offers a solution.

dynamic response of the blade.

Dynamic measurements are previously performed on small-scale coupon specimens with embedded piezoelectric sensors [10][11]. The measured output of the vibrating composite coupon in experiments is compared to analytic models. This way, dynamic strains are reconstructed to which the sensor response is modeled. By using predetermined strains in the experiments, the capabilities of piezoelectric sensors are better understood [12]. With this knowledge, sensors are potentially deployed in full dynamic strain reconstruction. An electro-mechanical coupling exists that is used for translating a strain field to the voltage output in a piezoelectric sensor. Huijer [13] designed and manufactured carbon fiber reinforced polymer (CFRP) specimens to assess among other subjects the ability of the embedded sensors to measure low-frequencies. Although the specimens are CFRP instead of glass-fiber reinforced polymer (GFRP), the research by Huijer is a useful foundation for expansion towards full-scale propeller research. The novel investigation of dynamic measurements on a full-scale FRC propeller blade with embedded piezoelectric sensors is the topic of this thesis. Due to low-frequency measurements, surface-mounted strain gauges are used to validate the proposed method.

1.2. Research question

The background information presents that composites potentially outperform metallic marine propellers in terms of efficiency and URN by hydro-elastic tailoring of the blades. Several methods can assess the extent of these potentials. Embedded sensing methods are convenient to use in dynamic response measurements of composites. This research prefers using piezoelectric sensors for their ability to operate in a broader frequency range. Two main observations stand out. First, piezoelectric sensors have previously been used in small-scale FRC specimens. Also, on full-scale marine propeller blades, non-piezoelectric sensors are used to assess the structure. These observations contain a research gap which is captured with a single research question:

> *How can the dynamic response of an FRC propeller be reconstructed by using embedded piezoelectric sensor measurements?*

1.3. Research subquestions

To elaborate further on the main research question, four topics are distinguished: full-field strain reconstruction, design of sensor embedment, experimental setup, and model assessment. Each topic includes subquestions to be answered to give more insight into this study.

1.3.1. Full-field strain reconstruction

The dynamic behavior of a flexible propeller blade is modeled in the design phase of the blade. After fabrication of the blade, it is desirable to monitor the dynamic behavior during operation and assess its correspondence with the modeled behavior. Monitoring in a non-destructive way is considered possible with a network of embedded sensors in the host material. A sensor network provides a reduced input while performance assessment requires a full-field output. To understand this relation, the following questions are posed:

> *How can full-field strain be reconstructed based on a network of embedded sensors?*

> *How can a finite element model of the blade be used in the analytic method of full-field strain reconstruction?*

1.3.2. Design of sensor embedment

The full-field response of the blade is assessed with a limited number of sensors. A suitable design of the sensor network is necessary for fabricating the FRC marine propeller blade. The quality of the measurements, the integrity of the sensors, and sensor cabling have to be studied. Two subquestions are posed to include in the design study:

> *How can a distributed network of piezoelectric sensors be embedded in an FRC marine propeller blade?*

How can the embedded sensors be localized and identified?

1.3.3. Experimental setup

An excitation on the FRC blade is necessary in order to measure structural responses by the sensor network. In this research, a free vibration test is executed. A subquestion is raised to study the relation of measurements to the dynamic properties of the blade:

How are dynamic properties of an FRC blade obtained by an embedded sensor network?

1.3.4. Assessment of analytical method

After experimental data is obtained, post-processing of the data is performed. The analytical model for full-field strain reconstruction has to be assessed. As validation, surface-mounted strain gauges are used in the experiments to measure unidirectional (UD) strain on the blade at specific locations. The following subquestions are formed related to the assessment of the analytical method:

How do the dynamic measurements by the embedded sensor network compare to both the strain gauges and finite element model?

1.4. Report structure

This research report is based on the structure shown in 1.1. The green outlined boxes indicate the chapter subjects. The orange boxes show the main procedures performed in the experiments and post-processing. Blue arrows are check-points to assess interim results.

In Chapter 2 the theory concerning piezoelectricity is discussed. In addition, the use of piezoelectric equations in setting up a reconstruction approach for the dynamic strain field of the blade is presented. Chapter 3 includes the design of the marine propeller blade with embedded sensors and the fabrication procedure. Chapter 4 describes the experimental setup and the execution of experiments. The results obtained from experiments are presented in Chapter 5. In Chapter 6, conclusions are drawn on the whole process with a focus on the experimental results. Discussion on the experimental setup and data, modeling, and application of the blade is done in Chapter 7 together with provided recommendations. This chapter also marks the end of the report.

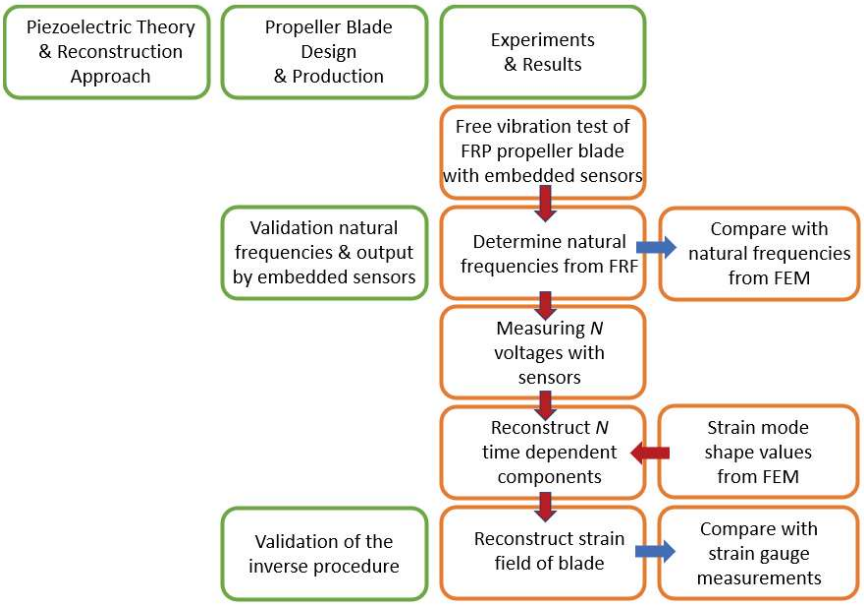

Figure 1.1: Global structure of current research

2

Theory & Modelling

This chapter is focused on the theory concerning the electro-mechanical coupling known as the piezoelectric effect. The voltage response provided by a piezoelectric sensor due to strain in the marine propeller blade is explained. In addition, an analytical model is proposed to invert the relation between voltage and strain. Hence, two subjects are distinguished as follows:

First, piezoelectric principles are discussed with governing equations. This discussion is finalized with the electro-mechanical relation and used assumptions. These assumptions are important in the low-frequency measurements performed in this research.

Secondly, both the forward and inverse procedures of electro-mechanical coupling are provided. An analytical model is proposed to reconstruct the strain field of the marine propeller blade. Modal properties of the blade are a significant aspect of the reconstruction. They are obtained from an FE model of the blade, which is discussed at the end of this chapter.

2.1. The piezoelectric effect

In 1880 the brothers Pierre and Jacques Curie already discovered that by applying pressure on certain crystals, e.g., lead zirconate titanate (PZT), an electric charge is created at the material's surface. A year later (1881), Gabriel Lippman predicted the inverse effect of this physical phenomenon. The so-called piezoelectric effect found its way into the scientific world, and both are discussed in this section with the corresponding equations. The focus lies on piezoelectric sensors embedment in an FRC marine propeller blade.

2.1.1. Piezoelectric sensors

The interaction between the electric charge and mechanical deformation is a linear relation for small strains and relatively low voltages and is mathematically described as such. Two phenomena are distinguished: the direct and the inverse piezoelectric effect. The direct effect is measured by covering a crystal with electrodes. Mechanical deformation of the crystal rearranges the crystal atoms and causes the positive ions to become dominant on one side of the material. Electrical neutrality does no longer hold, see Figure 2.1. Positive nuclei and negative electrons are unevenly distributed within the sensor from which a potential difference is created. The potential difference is measured in voltages.

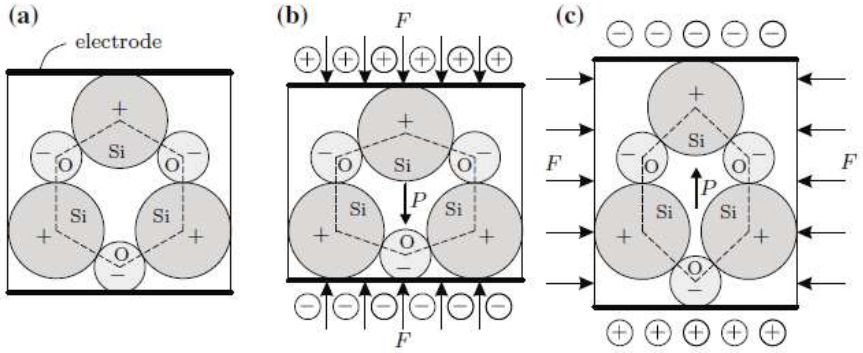

Figure 2.1: The schematic internal representation of polarization [14].

An external force can work on the crystal in the longitudinal, transverse, or shear direction. The direction of the force is not only visually represented but can also be physically related to the voltage output. The first law of thermodynamics is used to compute the change in internal energy U, see Equation 2.1.

$$\mathrm{d}\mathcal{U} = \mathrm{d}W + \mathrm{d}\mathcal{Q} = \mathrm{d}W_{\text{mech}} + \mathrm{d}W_{\text{elec}} + \mathrm{d}\mathcal{Q}_{heat} \tag{2.1}$$

In which W_{mech}, W_{elec}, and Q_{heat} are the mechanical energy, the electric energy, and the heat energy, respectively. With further elaboration on this equation, terms from Equation 2.1 are rewritten to Equation 2.2.

$$\mathrm{d}\mathcal{U} = T_{ij}\mathrm{d}S_{ij} + E_m\mathrm{d}D_m + \vartheta\mathrm{d}\mathfrak{s} \tag{2.2}$$

Where mechanical energy is described by the mechanical stress T_{ij} and the change in mechanical strain dS_{ij}. Also, the electric energy involves the electric field energy E_m and electric flux density change dD_m. The latter term in Equation 2.2 is providing temperature θ multiplied with the change in entropy $\mathrm{d}\mathfrak{s}$. Hence, the mechanical, electrical, and thermal linear coupling terms are represented.

Linear theory applied in piezoelectricity is described by Tiersten (1969) and is proved to be valid for any vibration on a piezoelectric resonator [15]. This theory formed the base for many other authors in piezoelectricity literature [16] [4] [14]. The focus on piezoelectricity relies on the linear relation, rate of change, mechanical strain, and electric flux density.

$$\begin{aligned} \mathrm{d}S_{ij} &= d^{\vartheta}_{ijn}\mathrm{d}E_n + s^{E,\vartheta}_{ijkl}\mathrm{d}T_{kl} + \alpha^{E}_{ij}\,\mathrm{d}\vartheta \\ \mathrm{d}D_m &= \varepsilon^{T,\vartheta}_{mn}\mathrm{d}E_n + d^{\vartheta}_{mkl}\mathrm{d}T_{kl} + \rho^{T}_{m}\,\mathrm{d}\vartheta \end{aligned} \tag{2.3}$$

With d^{ϑ}_{ijn} and d^{ϑ}_{mkl} as the piezoelectric strain and stress constants, respectively. The mechanical strain contains the elastic compliance constant $s^{E,\vartheta}_{ijkl}$ and the thermal expansion coefficient α^{E}_{ij}. The electric permittivity of the material $\varepsilon^{T,\vartheta}_{mn}$ and the pyroelectric[1] coefficient ρ^{T}_{m} are used to compute the electric flux density.

If the heat transfer from the surface of the propeller blade to the embedded sensor location is slow, an isotherm process might be assumed, see Equations 2.4 & 2.5. Future studies with the blade must further research this process to determine whether this assumption is justified.

$$\mathrm{d}S_{ij} = d_{ijn}\,\mathrm{d}E_n + s^{E}_{ijkl}\,\mathrm{d}T_{kl} \tag{2.4}$$

$$\mathrm{d}D_m = \varepsilon^{T}_{mn}\,\mathrm{d}E_n + d_{mkl}\,\mathrm{d}T_{kl} \tag{2.5}$$

Note that the subscripts denote the tensor rank. Rank notation isolates specific aspects of the equation and relates them to physical effects. While Equations 2.4 & 2.5 are known as the Sensing Equations, rewriting them with Hooke's Law gives the Stress Equations 2.6 & 2.7.

[1] Piezoelectricity exists in all non-centrosymmetric materials. Pyroelectricity is based a charge release due to a material's change of temperature. The latter occurs in materials of the polar crystal symmetry class.

$$\mathrm{d}T_{ij} = c^E_{ijkl}\,\mathrm{d}S_{kl} - e_{ijn}\,\mathrm{d}E_n \tag{2.6}$$

$$\mathrm{d}D_m = e_{mkl}\,\mathrm{d}S_{kl} + \varepsilon^T_{mn}\,\mathrm{d}E_n \tag{2.7}$$

Introducing the mechanical stiffness c^E_{ijkl} and the two electro-mechanical coupling coefficients e_{ijn} and e_{mkl}. The coefficients result from inverting the piezoelectric strain- and stress constants d^{ϑ}_{ijn} and d^{ϑ}_{mkl}.

These relations can be applied on the piezoelectric area of each sensor in the marine propeller blade. The mechanical strain working on the sensor should be equal to the strain in the blade. The electric displacement, also called electric flux density, is coupled to the mechanical strain in vector notation found in Gopalakrishnan et al. [12].

$$\left\{ \begin{array}{c} T_{ij} \\ D_m \end{array} \right\} = \varphi(\boldsymbol{x}) \left[\begin{array}{cc} c^E_{ijkl} & -\psi_{elec}(\boldsymbol{x}) e^T_{ijn} \\ \psi_{elec}(\boldsymbol{x}) e_{mkl} & \varepsilon^{\varepsilon} \end{array} \right] \left\{ \begin{array}{c} S_{kl} \\ E_n \end{array} \right\}, \quad \boldsymbol{x} \in \Omega \tag{2.8}$$

In which ψ_{elec} is a second function that allows the piezoelectric material to have different polarization on its area. In addition, it is noted that all mechanical terms consist of six components and the electric terms out of three components. By assuming electric displacement is dominant in the through-thickness direction and neglecting the other two directions, rewriting[2] this line from Equation 2.8 results in 2.9.

$$D_3 = \varphi(\boldsymbol{x}) b^T \left[\psi_{elec}(\boldsymbol{x}) d^{\sigma} c^E S + \left(\varepsilon^{\sigma} - d^{\sigma} c^E d^{\sigma^T} \right) E \right], \quad \boldsymbol{x} \in \Omega \tag{2.9}$$

The superscript σ indicates the property is measured at constant stress. The electric charge developed over the piezoelectric material area is zero in sensing mode, such that Equation 2.10 holds. After integrating the left and right sides of Equation 2.9 and applying Equation 2.10, the mechanical and electrical components are isolated as shown in Equation 2.11.

$$\int_{\Omega_P} D_3 \, d\boldsymbol{x} = \int_{\Omega} \varphi(\boldsymbol{x}) \, D_3 \, d\boldsymbol{x} \approx 0 \tag{2.10}$$

$$b^T d^{\sigma} c^E \int_{\Omega} S \, \varphi(\boldsymbol{x}) \, \psi_{elec}(\boldsymbol{x}) \, d\boldsymbol{x} = b^T \left(d^{\sigma} c^E d^{\sigma^T} - \varepsilon^{\sigma} \right) \int_{\Omega} \varphi(\boldsymbol{x}) \, E \, d\boldsymbol{x} \tag{2.11}$$

All material properties are assumed to remain constant over the whole sensor, and only through-thickness polarization holds. Hence, the electric field depends on the varying voltage over the sensor thickness, as shown in Equation 2.12. Substituting in Equation 2.11 results in Equation 2.13

$$E_3 = \frac{V}{t_p} \tag{2.12}$$

$$V = \frac{t_P}{A_P \left[b^T \left(d^{\sigma} c^E d^{\sigma^T} - \varepsilon^{\sigma} \right) b \right]} b^T d^{\sigma} c^E \int_{\Omega} S f(\boldsymbol{x}) d\boldsymbol{x} \tag{2.13}$$

In Equation 2.13, the integral depicts all strain components over the volume of piezoelectric material. The measured voltage is known as the forward approach. During this research, the inverse approach is studied. The applicability of Equation 2.13 in low-frequency measurements with piezoelectric sensors is discussed further in the next section.

2.1.2. Low-frequency measurements

The embedded system, or any piezoelectric sensor, can be described as a one-way coupling. This system is represented as an electric circuit including the sensor and a capacitor and resistor in parallel [10][14]. A formulation for this is given in Shin [11] and rewritten by Huijer [13] as shown in Equation 2.14[3]. It is based on Kirchhoff's current law.

$$F_S + F_{\vartheta} + C_s \frac{dV}{dt} + C_m \frac{dV}{dt} + \frac{1}{R_m} V = 0 \tag{2.14}$$

[2] The tensor ranks are left out for a clear representation of the equation. Also, symbol notation is kept constant between different authors.

[3] Equation 2.20 in Huijer [13].

With F_S and F_ϑ as current source terms, followed by the sensor capacitance C_s and the measured capacitance C_m. The last term in the equation includes the impedance R_m of the measured system multiplied by the voltage. It shows that multiple terms are time derivative dependent except for the voltage-resistance term. In low-frequency measurements, the time derivative limit goes to zero. Hence, the voltage decreases with decreasing frequency in order for Equation 2.14 to hold. This decrease indicates voltage leakage and thus electric discharge of the system. However, these electric discharge effects are neglected at typical and relatively high impedance values. This assumption, together with an isotherm environment of the sensor, leads to Equation 2.13.

It is concluded that the impedance of all components within the embedded system has to be analyzed. Huijer showed the differences between two impedance values in the low-frequency region. For the lower impedance, a decrease of voltage amplitude could be measured at frequencies from approximately 1.852 Hz and lower[4]. The current research aims to study a frequency range from 1-1000 Hz, which indicates the necessary impedance of the circuit components.

2.2. Vibration reconstruction approach

This section describes the forward and inverse relation between the strain and the principal coordinate vector. An analytical model is proposed with the potential to reconstruct the full-field strain.

2.2.1. Forward procedure

The electro-mechanical coupling is explained in Section 2.1.1 and partly covers the forward procedure of the piezoelectric effect. The strain components are used in computing a voltage output. However, the strains are unknown for any arbitrary loading condition. Therefore, a model is needed to describe the strain field in space and time, a vibration, to analyze the electro-mechanical coupling. A relation exists between deformation and strain. Equation 2.15 gives a formulation of deformation in space and time.

$$\vec{x}(x,t) = \sum_{i=1}^{n} \vec{\phi}^{(i)}(x)\vec{T}^{(i)}(t) \tag{2.15}$$

Equation 2.15 is solved by using the method of separation of variables, including two variables: space-dependent term $\phi(x)$ and time-dependent term $T(t)$ [17]. The space term describes the mode shape functions of the structure. Together with the natural frequencies, these functions are found by solving the eigenvalue problem of the marine propeller blade. For solving, the boundary conditions of the structure must hold. Since the blade has many boundary conditions due to its complex shape, it is more convenient to solve the eigenvalue problem using FE models, see Section 2.3. This research studies the contribution of each mode shape in a vibration. The contribution is attributed to the time component $T(t)$, described in Equation 2.16.

$$T(t) = A\cos\omega t + B\sin\omega t \tag{2.16}$$

In which A is the initial deflection at $t = 0$ and B represents the initial velocity of the beam at $t = 0$. Free vibration testing, which this research performs, involves only an initial deflection. Equation 2.16 is rewritten to Equation 2.17.

$$T_m(t) = A_m\cos\omega_m t \tag{2.17}$$

Where the subscript m indicates the time component is mode dependent. Each natural frequency has a contribution to the total structural deformation. In Equation 2.18, space and time components are related to their corresponding modes.

$$x(x,t) = \sum_{m=1}^{\infty} \Phi_m(x)\cdot T_m(t) \tag{2.18}$$

[4]Read Chapter 5 from Huijer [13].

The deformation is related to strain by taking the second derivative of the mode shape component. Also, the strain is evaluated to structural height with the term z. In Equation 2.19 the forward procedure is given to compute the strain in a bending beam in a two degree of freedom (DOF) system.

$$S(x,t) = -z \cdot \sum_{m=1}^{\infty} \Phi_{m,xx}(x) \cdot T_m(t) \tag{2.19}$$

The formulation shows that strain mode shapes provide the strain of an arbitrary location. An adaptation of this equation is shown in the proposed equation 2.29 for evaluating the full-field strain of the propeller blade. Furthermore, the term $T(t)$ - known as the principal coordinate vector - is unknown. Using Equation 2.13, the strain formulation is rewritten to isolate the principal coordinate vector.

2.2.2. Inverse procedure

This section discusses the combination of the forward piezoelectric effect and the strain computation. Reason for combining Equations 2.13 & 2.19 is the isolation of the principal coordinate vector. The principal coordinate vector is used to continuously monitor the governing frequencies in the vibrations of the marine propeller blade. First, Equation 2.13 is simplified to Equation 2.20.

$$V_n = h_n \cdot \int S \, d\Omega \tag{2.20}$$

$$V_n = h_n \cdot A_p \cdot S \tag{2.21}$$

In which h_n includes all electro-mechanical terms to describe the piezoelectricity of the sensor. The strain integral is solved by considering an averaged strain over the sensor area A_p since the sensor size is small compared to variation in strain. Equation 2.19 is substituted in Equation 2.21 to obtain a voltage output based on a two DOF strain.

$$V_n = h_n \cdot z \cdot \sum_{m=1}^{\infty} \Phi_{m,xx}(x) \cdot T_m(t) \tag{2.22}$$

It should be noted that from Equation 2.22, the electro-mechanical term is based on sensor area, which cancels out A_p. In addition, Equation 2.22 is a formulation solely based on the x-component of the strain mode shape. A model is presented to extend the voltage output on all directional components. The strain mode shape of the blade is computed in a finite element model (FEM), which is extensively discussed in Section 2.3. Also, matrix notation is used for the application of Equation 2.22 when multiple sensors are used, see Equation 2.24.

$$\psi_{n,m} = \begin{bmatrix} \Phi_{m,xx} & \Phi_{m,yy} & \Phi_{m,zz} & \Phi_{m,xy} & \Phi_{m,yz} & \Phi_{m,zx} \end{bmatrix}_n^T \tag{2.23}$$

$$\Psi = \begin{bmatrix} \psi_{1,1} & \cdots & \psi_{1,m} \\ \vdots & \ddots & \vdots \\ \psi_{n,1} & \cdots & \psi_{n,m} \end{bmatrix} \tag{2.24}$$

With vector $\psi_{n,m}$ containing the three principal directions and the three shear terms. The columns n and rows m represent the sensor quantity and the number of modes considered, respectively. The main modal matrix is multiplied with matrix H. The diagonal of this matrix is formed by the vectors h_n which is the electro-coupling of each sensor individually, see Equation 2.25.

$$H = \begin{bmatrix} h_1 & \cdots & 0 \\ \vdots & \ddots & \vdots \\ 0 & \cdots & h_n \end{bmatrix}, \text{ with } h_n = \frac{t_P}{\left[b^T \left(d^\sigma c^E d^{\sigma^T} - \varepsilon^\sigma\right) b\right]} b^T d^\sigma c^E \tag{2.25}$$

Matrix multiplication replaces the summation sign for which a coupling of values related to the same sensor remains. Equation 2.22 is rewritten to Equation 2.26. The inverse in Equation 2.27 can only be applied when the multiplication of H & Ψ results in a square matrix.

$$V = z \cdot H \cdot \Psi \cdot T(t) \tag{2.26}$$

$$\frac{1}{z} \cdot [H \cdot \Psi]^{-1} \cdot V = T(t) \tag{2.27}$$

A continuous analytical system shows that the inverse procedure can work. However, an under-determined problem is mitigated by computing six strain mode shapes components from a single voltage output. Also, a risk of ill-conditioning is added to such a procedure. Ill-conditioned systems are recognized by diagnosing a small change in input that causes a significant change in the computed solution. The model in this study aims to show that the inverse procedure holds for a multi-DOF system, such as the FRC marine propeller blade.

2.2.3. Strain field reconstruction

In practice, the strain is a function of space and time, such that $S(x, y, z, t)$. This indicates that strain has six dynamic components. These components consist of the three principal directional components and their shear components. The voltages measured by the reduced amount of sensor network each must be decomposed in these strain components. To study the decomposition of voltage and to compute a full-field strain, the following question is to be answered in this section:

How can full-field strain be reconstructed based on a network of embedded sensors?

In the previous section electro-mechanical coupling is discussed for an area of piezoelectric material. The coupling is used for multiple individual piezoelectric sensors with a limited number of embedded sensors in the FRC blade. Vectors and matrices are used to compute the principal coordinate vector, shown in Equation 2.28.

$$\begin{aligned} V_{full} &= H_{full}\, S_r \\ &= H_{full}\, \Psi_r\, T_{pcv} \\ T_{pcv} &= [H_{full}\, \Psi_r]^{-1}\, V_{full} \end{aligned} \tag{2.28}$$

n_s =	No. of sensors
n_t =	No. of time-steps
n_m =	No. of modes

Table 2.1: Definitions of matrix dimensions.

Where V_{full} is the voltage vector with size $[n_s \times n_t]$. All definitions of the matrix dimensions are shown in Table 2.1. The voltage vector is a multiplication of the full electro-mechanical coupling matrix H_{full} with the reduced strain field S_r. The coupling matrix is a diagonal-like matrix with size $[n_s \times 6n_s]$. The reduced strain field has a size of $[6n_s \times n_t]$. It is called a reduced field since only the strains at the location of embedded piezoelectric material are computed. In addition, it is emphasized that the size of S_r is six times larger than the voltage vector V_{full} due to the six strain components. The reduced strain field is decomposed in the reduced modal matrix Ψ_r and principal coordinate vector T_{pcv} with sizes $[6n_s \times n_m]$ and $[n_m \times n_t]$, respectively. The sensitivity of having fewer sensors than the size of vector T_pcv is to be studied since the system is then under-determined. Furthermore, the principal coordinate vector is used in Equation 2.29to compute the strain of an arbitrary point in the FRC blade.

$$S_{full} = \Psi_{full}\, T_{pcv} \tag{2.29}$$

n_{sdof} =	No. total nodes

Table 2.2: Full-field strain dimension.

In which S_{full} is the full-field strain matrix with size $[n_{\text{SDOFs}} \times n_m]$. The right side is a multiplication of the previously computed T_{pcv} and the full modal matrix Ψ_{full} with sizee $[n_{\text{SDOFs}} \times n_m]$.

The analytical method is set up to support the reconstruction by a FEM of the FRC propeller blade. The FEM is used for providing the reduced modal strain values at the estimated locations of the embedded sensors. The voltage vector results from experiments after which an analytical reconstruction model is proposed, as seen in Equation 2.29. For validation of the quality of the reconstruction, the measurements must be compared to an external method. Strain gauges are a convenient and suitable comparison since these gauges can be arbitrarily placed on the blade surface[5].

2.3. Finite element model

The previous section mentioned the significance of the reduced modal strain matrix in the reconstruction method. Therefore, the flexible propeller blade is modeled in a FEM. It is important to understand the involvement of the FEM in constructing this matrix. For this reason, the related subquestion is formed:

How is a finite element model used in the analytic method of full-field strain reconstruction

The FE model consists of multiple elements that form the structure's geometry and are assigned with both material properties and boundary conditions. This input is necessary to solve the eigenvalue problem of the marine propeller blade. The blade is discretized in order to limit the number of DOFs. An exemplification of a discretized marine propeller blade[6] is shown in Figure 2.2.

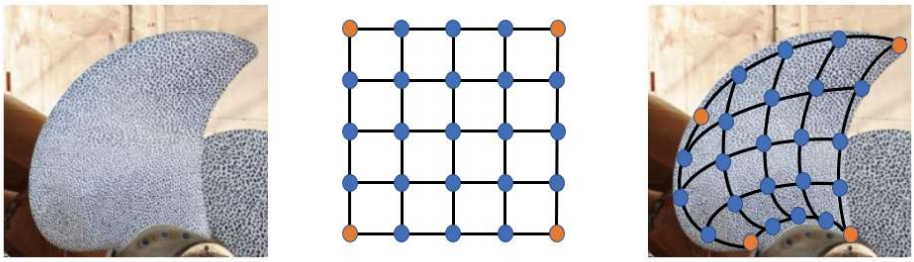

Figure 2.2: Propeller blade discretization (top view)

Previous research produced an FE model of a composite marine propeller blade in the program Marc Mentat. Results regarding static behavior were extracted from this model and compared with experimental results [2] [18]. The FE model is re-used in this current research, which extracts the dynamic properties from the FEM.

Two element types are distinguished in the FE program: an isotropic 20-node solid element (3D) to describe the core material and a composite 20-node brick element (3D) to describe the composite layers that form both faces of the propeller blade. These two element types are denoted by type 21 and type 150, respectively, and shown in Figure 2.3a. Hence, discretization is also used through-thickness of the structure.

[5]This excludes bending the strain gauges over the leading or cutting edge of the propeller blade. Logically, the gauges are sensitive to bending.

[6]The marine propeller blade as shown in Figure 2.2 is produced in the research of Maljaars [2].

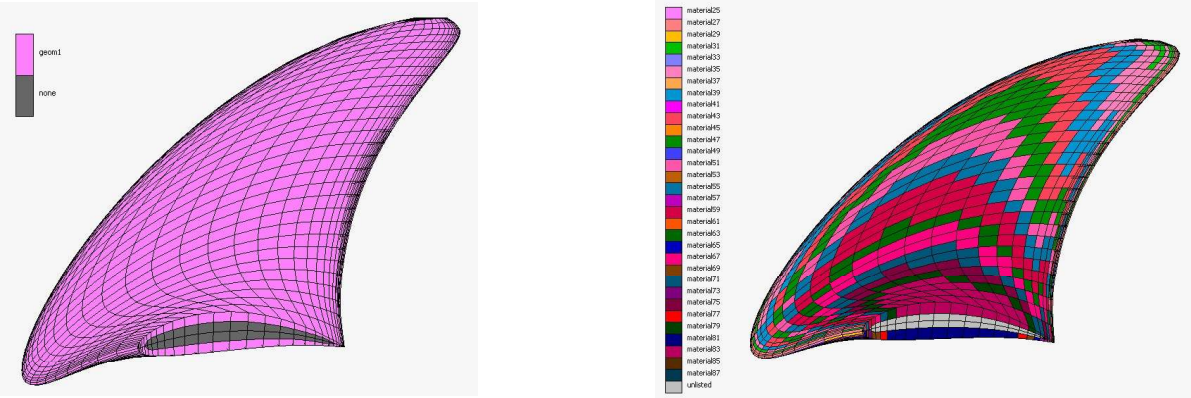

(a) Element types (21 and 150) of the FE model [18].

(b) Material distribution of FE model [2].

Figure 2.3: Defining the FEM in element- and material types.

Element type 21 is a polymat layer that adds a more convenient stiffness per mass ratio to the blade than FRC plies. Along the neutral axis of the blade, less to no stresses are expected. The elements of type 150 differentiate throughout the structure since the face elements of the propeller blade are not homogeneous. These elements each have different stacking sequences, or fiber-reinforced plies, since the thickness from root to tip of the blade decreases. Hence, the stacking sequence at the tip consists of fewer plies than the sequence at the root of the blade. In order to model these different stacking sequences, multiple material types are used as shown in Figure 2.3b.

Although the stacking sequence of the face elements differs, the strain and stress distributions of these elements are all computed according to the Classical Laminate Theory (CLT) [19]. The output of analyzes in Marc Mentat provides values at the four integration points of a single-ply in the stacking sequence of a specific element, see Figure 2.4. Gauss Quadrature is used to correctly model each ply in the element to its neighbor for smooth results over the complex shape of the blade. Hence, the strains at the node of an arbitrary element to the connecting node of a neighboring element should be equal.

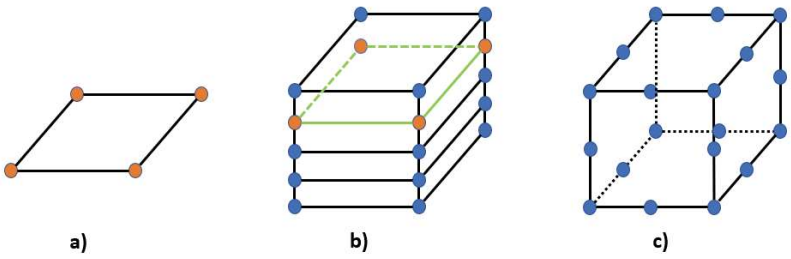

Figure 2.4: a) single ply, b) stacking sequence, c) 20-node element.

As mentioned, the FEM provides the strain mode shapes used in the analytical model of the strain field reconstruction. The strain mode shape is defined at the nodal points of the discretization. The output file of Marc Mentat gives the strain mode shape values at the four integration points of every single ply in all composite elements[7]. Also, these strain mode shape values are given for each mode shape under consideration. A selection matrix is applied to the data set to isolate the elements in which the piezoelectric sensors are embedded. These locations are described in Chapter 3. The strain values at these four points are averaged over the ply in the specified element, according to Cook [20]. Hence, Equation 2.23 can be filled for each embedded sensor and compose a modal strain matrix in Equation 2.24.

[7] The integration points of a single-ply are presented as orange dots in Figure 2.4.

2.3.1. Modal strain matrix

In Marc Mentat, a dynamic analysis is executed on the FE blade. The number of modes to consider in the analysis can be adjusted. Marc Mentat provides nodal stresses and strains of the structural modes, including the nodal coordinates. Preferred locations for sensor embedment are selected in a nodal 2D representation of the blade. The reduced modal strain values are computed at selected nodes in Marc Mentat, whereas voltage vector inputs are provided at the nodal locations from Rhino, see Table 2.3.

Ψ_r =	Marc Mentat	2D
V_{full} =	Rhino	3D

Table 2.3: Matrix dimensions of reconstruction method.

For convenience, the matrices Ψ_r and V_{full} are to be computed at the same node, and the nodes in Rhino have to be matched to the elemental nodes from Marc Mentat. Since the Rhino data is 2D, two principle coordinates are used in the least square function to find matching elements of Marc Mentat. The third coordinate is determined by the layer in which the sensor is embedded. There is a discrepancy on this related to different dimensions. Figure 2.5 shows both the Rhino and Marc Mentat presentations of selected sensor locations.

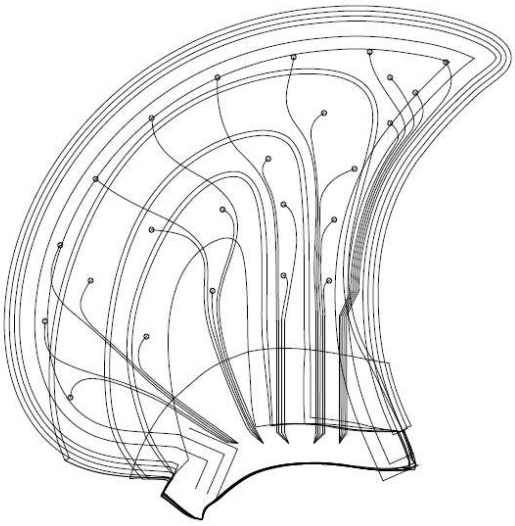

(a) Embedded sensor locations in 2D Rhino.

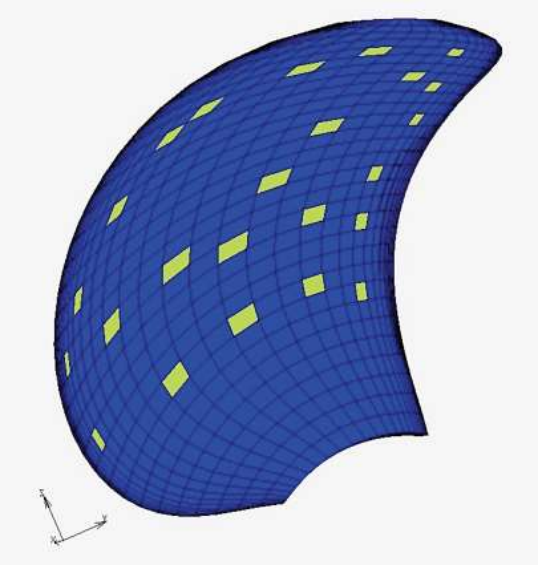

(b) Matched elements in 3D Marc Mentat.

Figure 2.5: Approach on matching coordinates of Rhino & Marc Mentat.

The selected elements in Figure 2.5b and their stresses and strains are defined in the global coordinate system. In experiments, the embedded sensors measure the local strains. Therefore, a rotation matrix is applied to each selected element to obtain the correct strains[8]. The strain modal matrix is constructed with strain mode shapes in the local coordinate system.

[8] A normal vector of each square element is defined. The out-of-plane normal component is coupled to the z-direction of the global coordinate system. It provides a rotation matrix that is unique for the local system of the square element.

3

Blade Fabrication

This chapter describes the pre-experiment process: fabrication of the marine propeller blade. Considerations made and discrepancies found during fabrication are discussed. Additionally, responsive measurements on the piezoelectric sensors after the fabrication process are described. The subquestions related to the design of sensor embedment are discussed in this chapter.

3.1. Blade design

The geometry for the FRC marine propeller blade used in this study is equal to that of the blade used in Maljaars [2]. The fabrication of the blade is executed as a vacuum-supported resin transfer moulding (RTM) process, see Section 3.1.5. Figure 3.1 shows the used top and bottom parts of the mould.

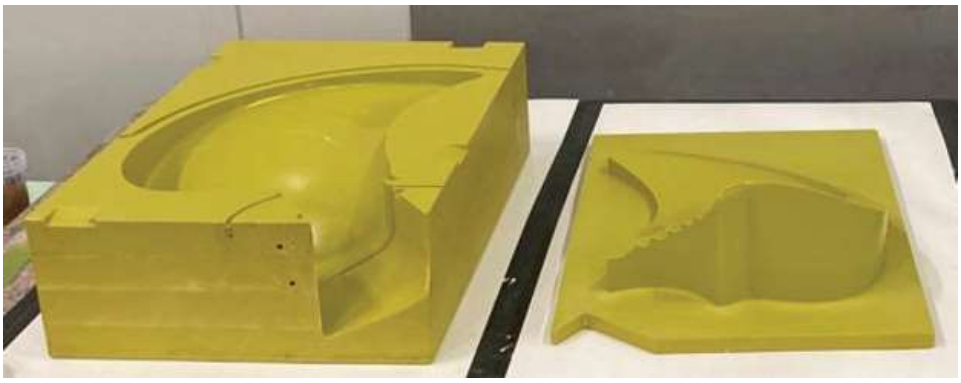

Figure 3.1: The closed mould used in the RTM fabrication process.

3.1.1. Stacking sequence

As described in Section 2.3, the strain mode shape matrix is derived from a FEM of a marine propeller blade. The voltage measurements of the piezoelectric sensors are executed in a real propeller blade. Since these two components are used together in Equation 2.29, the real blade properties must be in certain agreement with the FE blade. The material properties depend on the ply fiber directions in the laminate, used fibers, and used epoxy[1]. During fabrication, it is concluded that discrepancies exist between the laminate in FEM and the cutting plan used in fabrication. It is decided not to adjust the cutting plan but write down these discrepancies[2]. The differences in fiber directions are shown in Tables 3.1 & 3.2 for layers of the suction side. Zero degrees UD- and G-flow plies are not shown in the tables since no discrepancies occurred in these types. The use of G-flow is further discussed in Section 3.1.5.

[1] Fibres and epoxy of the FEM and real blade are in agreement. Maljaars matched product information with the FEM.
[2] It is assumed Maljaars received the same cutting plan and the natural frequencies showed significant agreement.

Layer no.	7	9	12	13	14	16	17	18	19	20	22	23	24	26	27	**[-]**
FEM	-20	-20	-20	15	15	60	60	105	60	60	15	15	-20	-20	-20	**[deg.]**
Measured	-15	-15	-20	25	15	60	-60	105	-60	-60	15	15	65	65	-20	**[deg.]**
Abs. diff.	5	5	0	10	0	0	120	0	120	120	0	0	85	85	0	**[deg.]**

Table 3.1: Suction side stacking sequence.

Layer no.	31	32	34	35	36	38	39	40	41	42	44	45	46	49	51	**[-]**
FEM	-20	-20	-20	15	15	60	60	105	-60	60	15	15	-20	-20	-20	**[deg.]**
Measured	-20	15	15	15	10	60	50	105	60	60	15	15	-20	-25	-25	**[deg.]**
Abs. diff.	0	35	35	0	5	0	10	0	120	0	0	0	0	5	5	**[deg.]**

Table 3.2: Pressure side stacking sequence.

Absolute differences higher than ten degrees are highlighted. An additional discrepancy is the gradual decrease of the thickness of the propeller blade from its hub to the edges: the leading edge, trailing edge, and the tip of the blade. The ply offsets in the FEM are not applied to the cutting plan. Therefore, the produced blade has an increased step size between consecutive zones compared to the FEM.

3.1.2. Embedding approach

Piezoelectric sensors are embedded between the plies of the blade laminate. This section describes the considerations on where the sensors are embedded. Therefore, it is aimed to answer the subquestion:

> *How can a distributed network of piezoelectric sensors be embedded in an FRC marine propeller blade?*

This answer includes multiple topics such as the embedding depth and plane location parallel to the blade surface. Also, the sensor wiring and the FRC marine propeller blade fabrication are crucial aspects of the network.

The embedding depth of the sensors is related to structural bending. In blade bending, the stress at the surface is higher than in a location close to the neutral axis. Hooke's Law states that stress is proportionally related to strain within the material's elastic limit. Hence, a sensor near the surface has more risk for failure, while a sensor near the neutral axis might not measure any strain. Both situations defeat the purpose of embedding piezoelectric sensors in an FRC structure. In addition, temperature differences at the surface of a marine propeller blade are present during operation. They can have a significant influence on the sensor measurements [21]. In this research, a constant percentage of embedding depth is applied. This way, sensing takes place at an approximate constant percentage [3] of total inertia. Another method exists in which all sensors are embedded in a SMART layer [22]. However, the constant embedding depth would be compromised. Also, the SMART layer is a pre-impregnated ply. This study uses dry fibers in the RTM fabrication process. This method is further described in Section 3.1.5.

In Huijer, compression loads on specimens with embedded piezoelectric sensors had a higher decrease in ultimate strength than tensile loads [13]. In a flexible marine propeller blade, the pressure and suction side are more likely to be under compression and tensile loads, respectively. Hence, it deems more convenient to have sensors embedded on the suction side of the blade. The sensors are structurally distributed within the blade to accommodate the measured output. Figure 3.2 shows prominent lines on a foil along which the sensors are embedded. It involves the trailing edge, leading edge, chord centerline, span centerline, and root. A more visible representation is previously shown in Figure 2.5.

[3] An approximate 32% percentage of the thickness is used for embedding in the suction side.

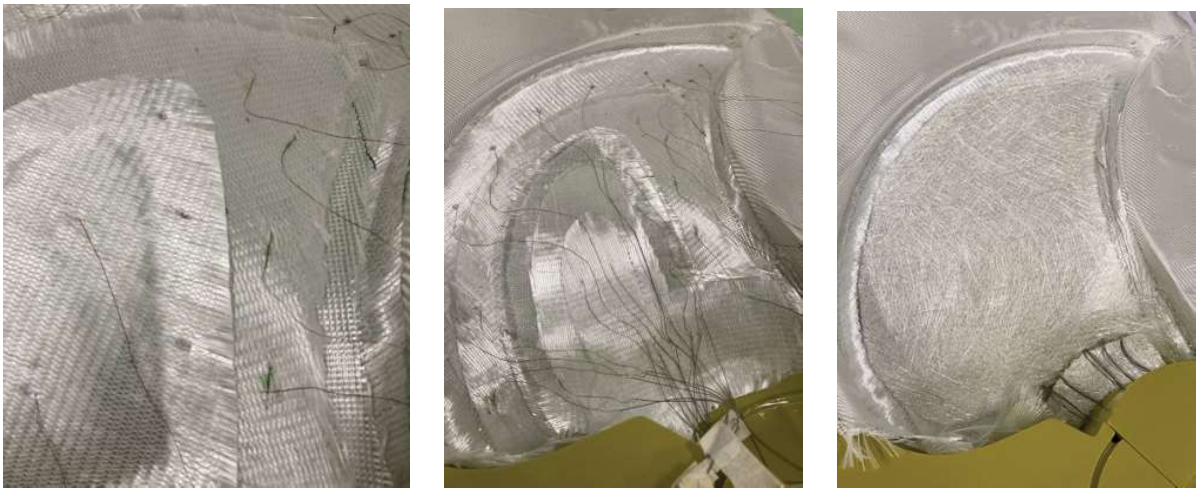

Figure 3.2: Sensor wiring between plies a) wire pulling b) finished layout c) covering suction side.

3.1.3. Sensor

The embedded sensors are manufactured by Piceramic© and are made of ferroelectric soft piezo material (PIC255). In addition, it contains silver electrodes. Twenty-four sensors of type PRYY+0398[4] are used. The Curie temperature of this material is approximately 350 degrees Celsius [24]. The resin has a curing temperature of around 210 degrees Celsius and is used since it does not reach the depolarisation temperature [25]. The material used for connecting the wires is lead-free solder called S-Sn95Ag4Cu1.

3.1.4. Wiring

With S-Sn95Ag4Cu1 solder, the bifilar enameled copper wire is connected to the top and bottom of the embedded sensors. In the soldering process, it is essential that the Curie temperature is not reached. Also, the wires are meandered through the plies, as shown in Figure 3.2. Meandering wires tend to decrease the risk of tensile loads on the wire. Namely, it is possible that the curing process of the composite shifts the embedded components. It is assumed that this risk is most significant at the root of the blade. The embedded wires come out of the FRC blade at the root to be connected to the data acquisition (DAQ) system. Coaxial cables are soldered to the copper wiring. In addition, insulation is applied to this soldered connection to prevent short-circuiting. The coaxial cable is thicker and assumed to have an increased bending resistance. All coaxial cables are positioned at the inside of the ply neighboring the core material.

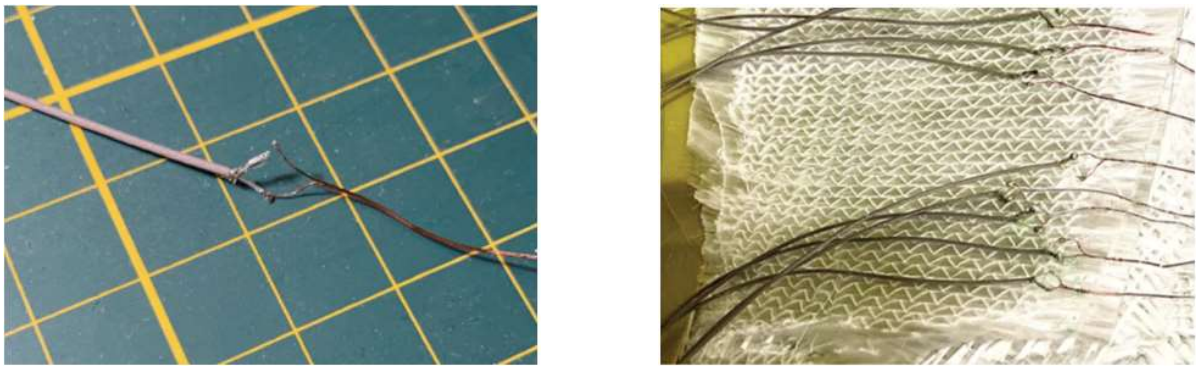

(a) Result of soldering copper to coax wire.

(b) Soldered wiring embedded in glass fiber laminate.

Figure 3.3: Approach on wiring considerations.

[4]Piezoelectric disc, outside diameter (OD) = 5 mm × thickness (TH) = 0.25 mm, piezo material PIC255, electrode Ag screen printed; disc c255 o5 t0.25 eAg[23].

3.1.5. Resin transfer moulding

The method used to fabricate the marine propeller blade is RTM. In RTM, the resin is transferred through a laminate of dry fibers. The transport of resin is possible due to a vacuum connected to a specific side of the mould. Hence, the resin is distributed over the product area. To ensure through-thickness distribution of the resin, plies of G-flow are added in the stacking sequence. The sensors and wires are embedded in dry fiber plies[5] of the suction side, the bottom part of the mould, after which the polymat layer covers these components. The polymat is the mid-ply and functions as the core material of the marine propeller blade. The plies of the pressure side finish the stacking sequence. The mould is closed, and a double vacuum is connected to it. The RTM process is schematically shown in Figure 3.4.

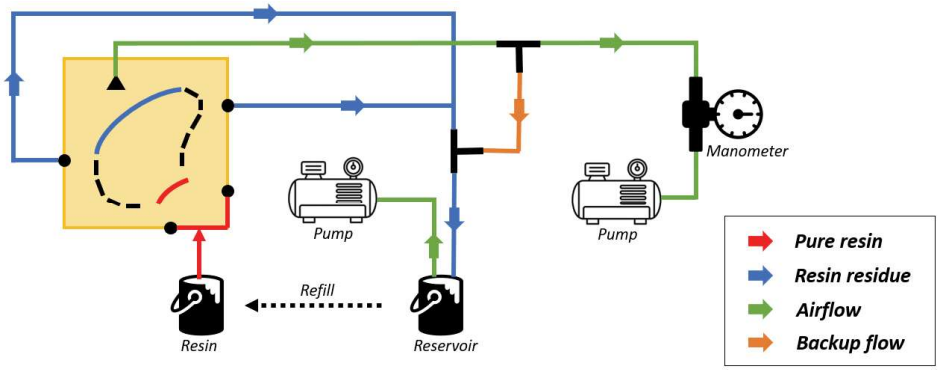

Figure 3.4: Schematic overview of vacuum-supported resin transfer moulding (VSRTM)

At the root side of the mould, there are two entrances (red) for the resin mixture. There are two exits (blue) at the other end through which excessive resin is transported. The transportation is triggered by the vacuum pumps (green). The pump on the reservoir starts the transferring of resin. The second vacuum pump presses the top and bottom parts of the mould against each other for a solid end product. The manometer measures the quality of the vacuum. The orange drain secures the vacuum within the system overnight when both pumps are turned off.

Once the blue drains contain resin, the resin is not already distributed over the entire blade. Resin takes the shortest route to the mould exit. The RTM process is continued for a total of 90 minutes. Measurements of pressure and temperature are executed. The measurements include the temperature of the resin mixture, the outer surface of the mould, the resin tube going in the mould, and the resin tube going out of the mould. The results are shown in Table 3.3.

	Part I				Part II			Part III			Unit
time	00:30	00:38	00:46	00:52	00:58	01:04	01:10	01:18	01:24	01:30	[h]
P	[-]	27,2	21,3	20,8	[-]	20,8	20,8	20,8	20,8	20,8	[hPa]
T_{resin}	22,0	[-]	23,0	23,4	22,3	23,7	22,6	21,7	22,5	21,8	[deg]
T_{mould}	18,4	[-]	18,6	18,3	17,4	17,8	17,4	17,0	17,0	17,3	[deg]
$T_{tube,in}$	[-]	[-]	19,6	19,3	18,4	18,5	18,8	18,1	18,4	18,2	[deg]
$T_{tube,out}$	[-]	[-]	19,0	18,6	17,5	17,8	18,1	17,4	17,3	17,7	[deg]

Table 3.3: Data measured over time during the RTM process.

The table indicates a stable process for the time duration of the surveillance. For the pressure on the supporting vacuum bag, this is preferable. Either the vacuum pump does not have enough power to

[5]Dry plies are more convenient than pre-impregnated plies since prepreg plies are already covered in resin. Wet plies make wire pulling through these plies more difficult. Additionally, prepreg ply rolls are stored in cool environments to ensure their shelf life, limiting the available time for fabrication. Similar arguments hold for the use of wet layup.

increase the vacuum, or it does not overcome the minor leakage along the vacuum bag. The pressure value is deemed enough for the RTM process. It is expected that the temperature of the resin would have increased in the measuring period of 90 minutes since the process is exothermic[6]. It is recommended to monitor the temperature for a more extended period in future fabrication until the peak temperature is reached. This way, it can be ensured that the preferred properties of the composite are obtained. Namely, the curing temperature influences the cross-linking of the polymer. The temperature values for the mould and in- and outgoing tubes show a minor thermal decrease. Since multiple aspects affect the tubing and mould surfaces, no significant influence on the RTM process is assumed.

3.2. Sensor integrity and identification

The study aims to obtain voltage measurements from the embedded sensors. Hence, it is necessary to assess whether the embedded sensors are responsive. After curing the FRC marine propeller blade, it is impossible to physically reach the piezoelectric sensors without damaging the structure. This obstructs the ability to assess the network quality concerning voids between the sensor and host material. However, the responses of the sensors are assessed via the wiring system.

In Section 2.1.2 the assumptions for low-frequency measurements are discussed. It is concluded that in low-frequency measurements the impedance is dominant. These aspects are derived from Kirchhoff's current law, given in Equation 3.1 & 3.2 [4].

$$\sum I = 0 \tag{3.1}$$

$$I_s + I_m = 0 \tag{3.2}$$

In which I_s and I_m are the currents of the sensor and external elements in the circuit[7]. The current is given as the rate of charge Q. Equation 2.10 shows that Q is the surface integral of the electric displacement over piezoelectric material. Combined with the definition of sensor current from Equation 2.14 this provides Equation 3.3:

$$I_s = \frac{d}{dt} \int D \, dA = C_s \frac{dV}{dt} \tag{3.3}$$

$$C = \frac{\varepsilon_{pv} \cdot A_p}{d} \tag{3.4}$$

Equation 3.4 is derived for computing the capacitance of a circuit. In which ε_{pv} is the permittivity in vacuum and d is the distance between the sensor plates. The cross-sectional area A_p of the wire contributes to the potential capacitance of the wired system. These equations show that the integration area influences the relation between the capacitance and electric displacement. In addition to the sensor, each component in the system contributes to the integration area. In Chapter 5, the results of the capacitance measurements after adding a component to the circuit are provided.

[6] The exothermic reaction is not linear, and it is possible that the temperature rapidly increased after 90 minutes.
[7] This sensor current includes wiring, solder material, and breadboard. See Section 4.1.

4

Experiments

4.1. Vibration test setup

In order to obtain vibration measurements from embedded piezoelectric sensors, the blade is excited with an external impact in the experiments. This section describes the considerations used in the test setup of the FRC marine propeller blade.

4.1.1. Blade mounting

Conventional design shows that the propeller blades are clamped to a hub to form a complete marine propeller. This research involves the production and testing of a single blade. It is crucial to determine the boundary conditions of the structure. As mentioned in Chapter 2, the conditions used to obtain the strain modal matrix must equal those in the voltage measurements. While the FE blade is modeled as a free object, the same free conditions must be used in the test setup. The freely-hanging blade with a single-point attachment is shown in Figure 4.1. Although the attachment may attain a certain stiffness, this is neglected in the modal analysis and reconstruction.

Figure 4.1: Single-point suspended FRC blade for free vibration tests.

Two excitation methods are distinguished in modal analysis: forced and free vibration. Modal analysis was performed on a composite marine propeller blade in air and water in previous free vibration tests. It is concluded that a significant decrease in natural frequencies is found in water [2]. The added mass[1] is up to six times higher than the mass of the composite blade [26]. The current research is focused on free vibration of an FRC marine propeller blade in air. This medium is convenient for the sake of assessing the sensor working and applicability[2]. It is aimed to include the longitudinal, transverse, and torsional vibrations in the analysis.

[1] Added mass is additional inertia given to a system due to the movement of a structure - the blade - through a fluid. The fluid volume surrounding the structure is displaced or deformed as well.

[2] Experiments in water would increase the risk on short-circuiting of the sensors and insecurities in computing the previously mentioned added mass.

4.1.2. Measurement system

The entire electric circuit of the measuring setup is discussed and shown in Figure 4.2. The components in the setup are briefly described.

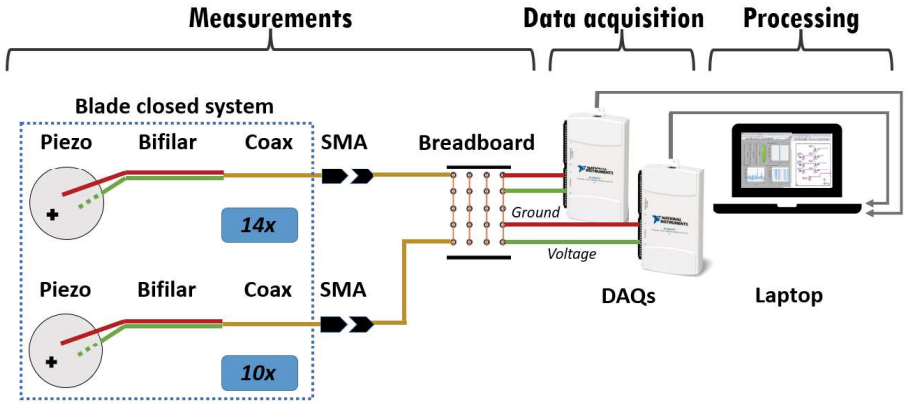

Figure 4.2: Schematic overview of the measurement setup.

Measurements

As a response to the excitation of the blade, strains are imposed on the embedded sensors. These strains are the cause of the piezoelectric effect as described in Chapter 2. A voltage is sent through the wired system embedded in the FRC marine propeller blade. The coax cables come out of the closed system - indicated by the dashed blue boxes in Figure 4.2 - at the blade's root. The end of the coax cables is provided with an SMA connector. Via a breadboard and jumper wire, the voltage signal is processed by the DAQ system.

Data acquisition system

The DAQ used in the current study experiments is the NI USB 6211. It provides digital signals to the computer by converting the analog voltage signals.

Data processing

The digital signals provided by the computer are captured in LabVIEW. This program visualizes the data in graphical content. In addition, the data is saved for processing. Voltage vectors can be computed from the data and used to reconstruct the principal coordinate vector.

4.1.3. Strain gauge positioning

A second method is needed to compare results to validate the reconstruction of the full-field strain as proposed in Chapter 2. Surface-mounted strain gauges are widely applied and accepted methods, both as individual and comparison studies [11]. Strain gauges are used to measure the surface strain in a preferred direction. Conventionally, strains at the surface are higher than those near the neutral axis of the structure. Hence, a through-thickness correction is applied to compare strain gauges with embedded sensing methods. This allows for fair comparison.

A disc-shaped piezoelectric sensor has sensitivity in all directions, while the surface-mounted strain gauge measures strain unidirectional. Therefore, the coordinate system of the piezoelectric sensors follows the coordinate system as defined in the FEM. This allows for easier decomposition of the strains in the model. For a more accessible comparison, the UD strain gauges must coincide with either the coordinate system's y- or z- component in FEM. Therefore, two measurement series are set up: Serie A and Serie B. Strain gauges of Serie A are placed such that their direction coincides with the z-component of FEM. Serie B contains strain gauges that are put on the blade such that their direction coincides with the y-component of FEM. In Figure 4.3, all embedded piezoelectric sensors are numbered. The strain gauges are placed directly above the embedded sensors for comparison.

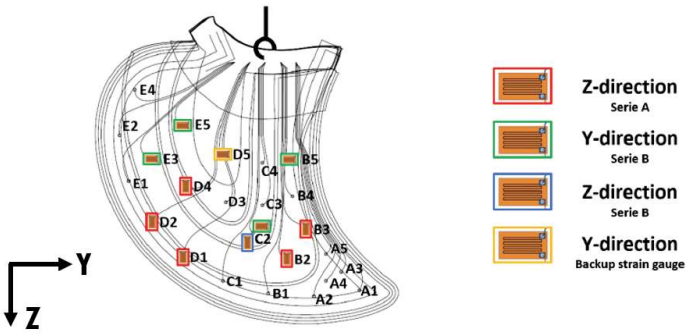

Figure 4.3: Sensor numbering and strain gauge directions.

As described in Chapter 2, an isotherm process is often assumed. However, the measurements by the surface-mounted strain gauges can be influenced by changing room temperatures in between experiments. To prevent possible deviations, this study uses a full Wheatstone bridge for each strain gauge.

Wheatstone bridge

The principle of the Wheatstone bridge is represented in Figure 4.4. Two lines A-C-D and A-B-D are parallel to each other. Both lines consist of two gauges and only line A-B-D has the blade mounted strain gauge. Additionally, these lines have to be balanced for current and voltage. Hence, when a bridge connection is applied between C and B, the current and voltage over this line should equal zero. If not, gauge R_v with a variable impedance is adjusted until this condition holds. Furthermore, the other gauges have to be applied on similar material as the blade mounted strain gauge. The similar thermal properties of the material make temperature calibration possible.

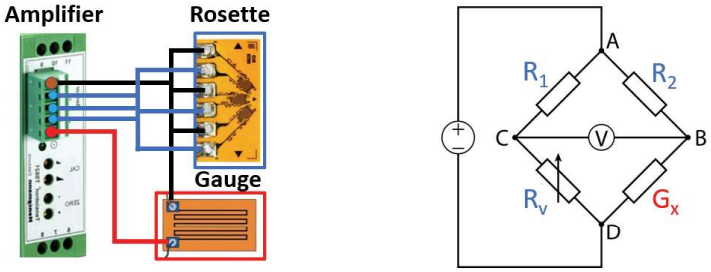

Figure 4.4: Overview of Wheatstone setup

Logically, the surface-mounted strain gauge G_x is on the FRC blade and the three other gauges R_1, R_2, and R_v are mounted on a substitute FRC specimen. In this experimental setup, a rosette is used in the Wheatstone bridge. Rosettes are composed of three strain gauges and thus convenient to use in this Wheatstone bridge setup[3] . The strain gauge amplifier[4] is the power system and contains the systems acquisition and impedance compensation. After that, the strain per voltage is computed such that strain values are obtained from voltage data. The method for computing initial strain is shown in Equation 4.1.

$$\begin{aligned} GF &= \frac{\Delta R/G_x}{\Delta L/L} = \frac{\Delta R/G_x}{\varepsilon_0} \\ \Delta R &= G_x - R_v \\ R_v &= \frac{R_s \cdot G_x}{R_s + G_x} \end{aligned} \tag{4.1}$$

[3]The unidirectional strain gauge type is CEA-06-125UWA-350 [27] and the rosette type is the CEA-06-125UR-350 [28]. Rosettes measure two unidirectional strains perpendicular to each other and their shear component.

[4]The strain gauge amplifier is type CPJ/CPJ-25 [29].

With known inputs for Equation 4.1 shown in Table 4.1:

R_s =	Impedance of amplifier	$= 269600\ \Omega$
G_x =	Impedance of blade gauge	$= 350\ \Omega$

Table 4.1: Definitions of impedance values.

In this equation, the Gauge factor (GF) is the fractional change $\Delta R/G_x$ of the impedance to the strain. Term R_v is the adjustable impedance. The GF[5] of the used strain gauges is averaged at $2.1\ [-]$. It should be noted that metallic strain gauges are used on glass fiber material. The metallic strain gauges that are used have a strain range of $\pm$ 5%. The strain range of glass fiber is measurable with these strain gauges [30][31]. Strain ε_0 is the initial strain that is imposed on the strain gauge. This value is divided over the static voltage U_1 of gauge G_x. Static voltage U_1 is corrected for voltage leakage U_2 over the amplifier, see Equation 4.2.

$$\Delta U = \mid U_1 - U_2 \mid \tag{4.2}$$

U_1 =	Voltage over strain gauge
U_2 =	Voltage over amplifier

Table 4.2: Definitions of static voltage gauges & amplifiers.

A ratio is obtained for each strain gauge mounted to the propeller blade to express voltage in strain. Equation 4.3 shows this relation with use of Equations 4.1 & 4.2.

$$C_{sv} = \frac{\varepsilon_0}{\Delta U} \tag{4.3}$$

The ratios C_{sv} for each mounted strain gauge are found in Table 4.3.

	Blade mounted strain gauges				
	B3	B2	D1	D2	D4
U_1	9.88	7.35	9.88	9.50	9.28
U_2	0.05	0.24	0.00	-0.15	0.07
ΔU	9.83	7.01	9.88	9.65	9.21
C_{sv}	62.7	88.0	62.4	63.9	67.0

Table 4.3: Voltage to strain ratios for blade gauges.

The table shows only the values for the strain gauges of Serie A placed in z-direction as represented in Figure 4.3. These strain gauges are used in the excitation experiments.

4.2. Impact testing

In free vibration tests, an initial impact is used to impose a deflection in the blade. The FEM executes modal analysis with the given boundary conditions. In the experiments, an impact is imposed at a known location on the blade with an impact hammer[6]. The hammer is connected to the DAQ system, together with the remaining piezoelectric sensors and the mounted strain gauges. It is expected that all responses are shown in LabVIEW for data processing.

[5] This value is found in product description.
[6] The Kistler 9726A5000 impulse force hammer [32]

Although the amount of surviving sensors is known, the connected cables from the blade are not yet matched to the corresponding sensors since the labeling got illegible after fabrication. Since it is crucial to match the responses with their location on the marine propeller blade, the following subquestion is posed:

How are the embedded sensors localized and identified?

The localization provides more insight into any translation of the embedded sensors during fabrication. The identification is used to match the measured response to sensor locations. Consecutively, the sensor locations are coupled to the elements from FEM, after which the modal strains are isolated from the output file.

Pressure is applied manually to the locations where piezoelectric sensors are possibly embedded. This is repeated for each group of sensors[7] individually. The sensor with the highest amplitude in the response signal is detected and identified. With a limited or absent response, the sensor at which pressure is applied is expected to be damaged. The results for this identification are shown in Chapter 5.

4.3. Vibration reconstruction

The study aims to provide more insight into the structure's dynamic behavior and integrity with the identified sensors. Since this is the first time[8] a network of embedded piezoelectric sensors is used in a full-scale application for this purpose, the subquestion states:

How are dynamic properties of an FRC blade obtained by an embedded sensor network?

The input for reconstruction is bounded to a limited amount of embedded piezoelectric sensors that provide response measurements. Reconstructing the full-field strain with a limited input is possible in structural health monitoring (SHM) [33][34]. If a full-field strain is obtained for the propeller blade, the quality of the resulting strains must be assessed. Reconstruction methods can be verified with a FEM or sensing methods. Therefore, a research subquestion is posed regarding verification:

How do the dynamic measurements by the embedded sensor network compare to both the strain gauges and finite element model?

The dynamic response of the individual embedded sensors is analyzed after excitation with the impact hammer. This response is an oscillation of voltage analyzed in the time or frequency domain. A similar analysis is available for the excitation since the hammer is also connected to the DAQ system. In the time domain of the excitation, an isolated peak is expected as the voltage amplitude caused by the impact[9].

Both responses can be translated from the time domain to the frequency domain using a Fast Fourier Transform (FFT). The response is quantified by a frequency response function (FRF) in the frequency domain. The FRF is mainly expressed in voltage magnitude in this study. Graphical representation of the FRF is convenient in determining the resonant frequencies of a structure. These resonant frequencies are not directly formulated as the natural frequencies of the blade. It is possible that the response is contaminated by components of the electric circuit, voids surrounding the piezoelectric sensors.

[7] Two channels survived in Group E, which contains five embedded sensors. A response is expected for only two embedded sensors after applying pressure at their location.

[8] At time of writing, no literature is known to the author that covers this exact topic.

[9] It must be ascertained that second or even more peaks are not retrievable in the response time domain. If more peaks are noticed, it might indicate that the excited blade bounced back and made contact with the hammer multiple times. This leads to contaminated responses in the frequency spectrum in case a single impact in the analysis is preferred.

5 Results

Results of the experiments are presented in this chapter. The topics discussed include the integrity and identification of the embedded sensors. In addition, results of the measurements with embedded piezoelectric sensors are shown. The individual results of the strain gauge measurements of Serie A are presented. Finally, an assessment on their correspondence with the mode shapes computed by FEM is performed.

5.1. Sensor integrity and identification

The network consists of 24 embedded piezoelectric sensors. After the curing process of the composite blade, the network is assessed via the wires connected to the embedded sensors.

5.1.1. Capacitance measurements

To assess the fabrication process, quality control of the circuit components is performed. This includes the capacitance of the sensor systems[1] and the ability of the breadboard to transfer the voltage signal. The reference capacitance of the individual sensors is set at 0.992 nF [23]. In Appendix B the capacitance measurement results are shown.

The average capacitance of the circuit, including only the piezoelectric sensor and the soldered bifilar wire, is measured at 1.16 nF. This magnitude was verified with capacitance measurements from previous research [13]. The capacitance of the circuit after soldering the coax cables averaged at 1.29 nF. The capacitance difference over these two soldering steps is computed. Only one sensor system with coax suffered a decrease in capacitance. Two coax systems measured an increase above 25%, which might be caused by excessive use of solder. Overall, the average increase after adding the coax cables is 11%. To understand the increase of capacitance, the previously used Equation 5.1 is analyzed. The distance between the sensor plates is assumed to remain unchanged after having soldered. However, the cross-sectional area might have increased from bifilar wire to the coax cables. Additionally, the two soldered components have different dielectric constants. Lastly, the wiring length contributes to charging effects, but this effect is not significantly represented in the data. Despite these minor discrepancies, the final system is concluded to be intact and suitable for application in voltage measurements.

$$C = \frac{\varepsilon_{pv} \cdot A_p}{d} \tag{5.1}$$

The breadboard has SMA connectors plugged in to transport the signal from the embedded sensors to the DAQ system. To verify that the SMAs and breadboard are correctly connected, the system's impedance is measured. The first measurement is a short-circuit between the inner lead of the SMA and the jump wire connected with the SMA core via the breadboard, where an average impedance of $0.4\,\Omega$ is measured. The second impedance measurement is done between the SMA core and breadboard ground. The overload shown on the multi-meter indicates an impedance at least higher than $10^6\ \Omega$. Both measurements on all SMAs showed the expected results.

[1] Sensor system refers to the piezoelectric sensor including the soldered copper and coax cable.

5.1.2. Embedded sensor survival

The result of the fabrication process demonstrates the influence of the RTM process on the survival rate of embedded sensors. The RTM process is initiated after the capacitance measurements. It shows that out of 24 embedded piezoelectric sensors, 13 sensors were intact after curing. For the 11 circuits that fractured during fabrication, three possible points of failure are present in the circuit: the piezoelectric sensor, the wire, or the solder connection. During this fabrication, all circuits failed on the coax wire. To capture the feasibility of fabrication and measurements, the subquestion is introduced:

> *How can a distributed network of piezoelectric sensors be embedded in an FRC marine propeller blade?*

From Chapter 3, it is concluded that piezoelectric sensors and the soldered wires can be embedded in between glass-fiber plies of the FRC marine propeller blade. For this study, all piezo-sensors are embedded on the suction side of the blade. Tweezers are used to open a space between pairs of perpendicular fibres. The opening through which the wires of the embedded sensors are pulled are conveniently closed by the same tweezers. Eventually, the end of the wires continue up to the polymat layer. The wires are assembled at the root of the blade within the polymat layer.

The failed circuits all fractured during the demoulding process, indicating a different approach for future fabrication should be implemented. However, the surviving circuits prove that piezoelectric sensors are responsive in capacitance. Since the measurements are in certain agreement, a surviving circuit is expected to maintain an intact sensor, wiring, and soldering.

5.1.3. Identification of embedded sensors

An amount of 13 embedded sensors survived fabrication and have to be localized and identified. Localization is performed to see whether the sensors drifted from their original location during the curing process, in a macro computed tomography (CT) scanner[2] [35], the blade was exposed to make a Rontgen-photo. The result of this scan is shown in Figure 5.1a. Comparing the sensor locations from the CT scan with Figure 2.5ashows that no significant displacements took place during production. The localization of embedded sensors is found to be successful.

(a) Macro CT machine with FRC blade.

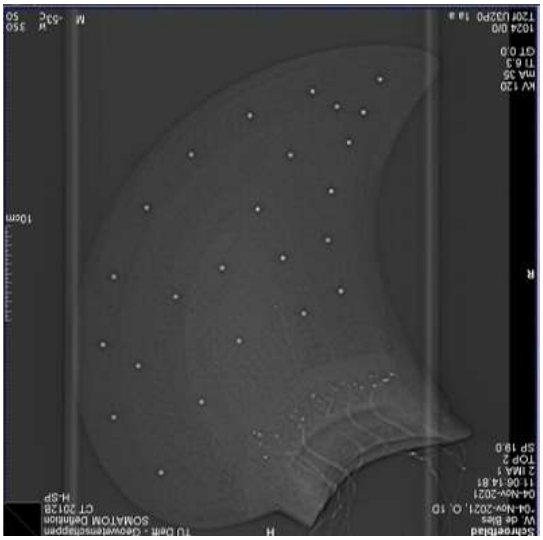

(b) Result of CT scan with identified sensor locations.

Figure 5.1: Localization of sensors with the Macro CT machine

Prior to closing the mould, each sensor is tagged with its letter and number as provided in Figure 4.3. The tags are compromised in the process as is described in Appendix E. Hence, the 13 sensors that are intact have to be identified such that these sensors can be labeled again. This is important considering

[2]The machine is located at CiTG, Delft University of Technology.

the matrix multiplication in the analytical method. The sensors with fractured wires can not be used in the reconstruction method and have to be left out of the modal strain matrix.

A systematic approach is used to confirm the identity of the working sensors. One after another, an individual group of sensors is selected and connected to the DAQ via the breadboard. Their locations are marked on the outer surface of the real blade suction side using Figure 5.1b. By applying pressure on the blade surface at a marked location, each connected sensor's voltage response over time is shown in the specified group. The approach of this procedure is demonstrated for sensor group E in Figure 5.2. Once a sensor system provides the highest response after applying pressure at a marked location of that group, the sensor system is labeled again.

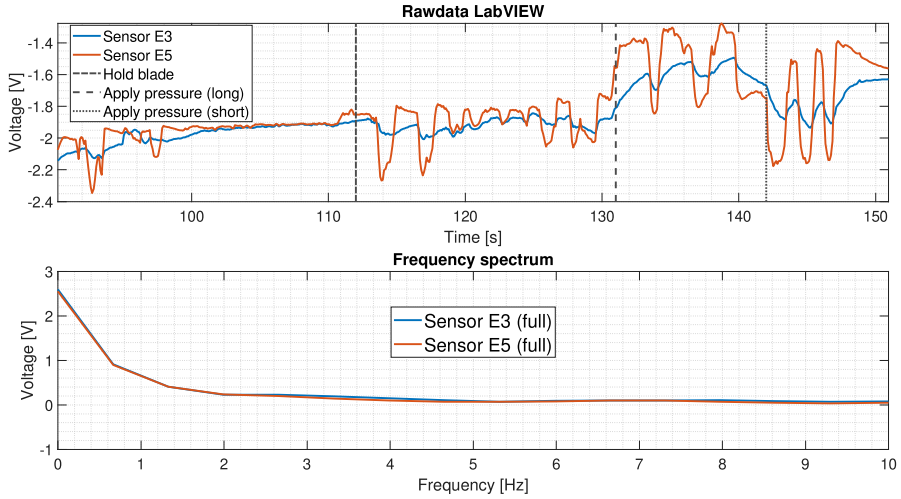

Figure 5.2: Identifying sensors 3 & 5 from Group E.

The data is shown after 90 [s] since that is the stabilization time of this experimental run. It is noted that the sensors start at a negative voltage of approximately -2 [V]. At 112 [s], the blade is held manually for a comfortable grip[3]. It explains the responsive behavior of the signal. At 131 [s], pressure is applied for approximately 2 [s] on the blade three times. These relatively long responses are followed by shorter responses. The latter is a consequence of applied pressures with shorter time intervals. Each pressure, long and short, is applied on the surface under which Sensor E5 should be embedded. The high responsive behavior of piezoelectric Sensor E5 compared to Sensor E3 implies that identification succeeded.

Figure 5.2b shows signal data of both sensors in the frequency domain. The density shows to be in the low-frequency region for both sensors. This is convenient since the pressures are also applied at low frequencies. It should be considered to remove frequencies lower than 0.1 [Hz] regarding the time derivative components in Kirchhoff's Law. Discrepancies in the response signal might become significant at frequencies lower than 0.1Hz.

As an answer to the subquestion:

How are the embedded sensor localized and identified?

Localization is performed with a CT scan and functions as a verification of the fabrication method. The sensor positioning is in agreement with the designed sensor layout as previously shown in Figure 2.5a. The deviation between the actual and proposed sensor location during blade fabrication is considered minimal. The approach of imposing manual pressure to match connected wires to the correct embedded sensor provides additional verification of the sensor identity and location.

[3]This way, it is easier to apply the pressure manually.

5.2. Results of piezoelectric sensors

This section describes the input signal imposed by the impact hammer and the responses of the ten embedded piezoelectric sensors. The FRC propeller blade is excited[4] with the tip of the hammer at impact location I_{loc}, see Figure 5.3. Both the excitation and responses are captured and visualized. This makes an assessment on the experimental results possible. The assessment includes the creation of FRFs. These FRFs are used to obtain the propeller blade's natural frequencies and mode shape.

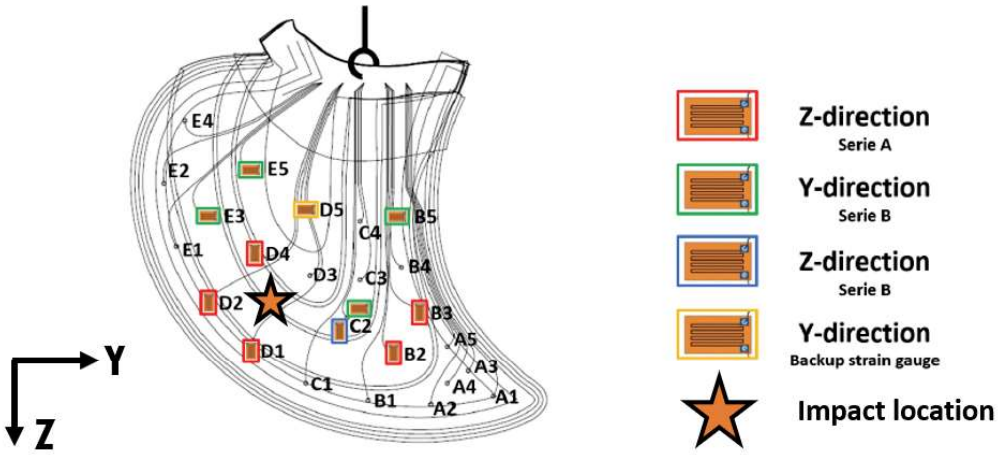

Figure 5.3: Impact location I_{loc} on the suction side of the blade.

5.2.1. Input signal measurements

The input signal is analyzed each time the blade is hit. For each hit, a separate data file is made. This is important since the input signal significantly influences the system's response. This study expects the input signal to contain a single impact in the time domain, assuming the propeller blade is hit once. Additionally, a single impact is convenient because this enables straightforward modal analysis[5]. The input signal is measured in voltage[6] and shown in Figure 5.4. Furthermore, the figure shows the output signal of piezo-sensor E5.

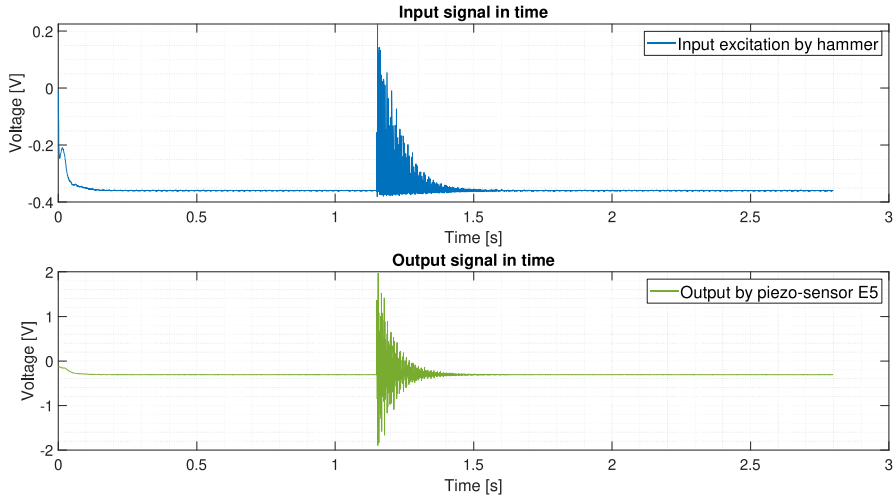

Figure 5.4: Unfiltered in- and output after excitation.

[4]The impact location does not coincide with the center chord-line or span-line of the propeller blade
[5]The analytical method is easier to validate based on a single loaded system than a multiple loaded system.
[6]The impact hammer is calibrated at 1.09mV/N. The input signal can therefore be expressed in either Newtons or Volts.

The raw data shown in Figure 5.4 is sampled at a frequency of 2000Hz. The output signal shows the conventional attenuation. However, it is striking that the input signal is of similar duration as the output by the embedded sensor. Although the propeller blade is assumed to be hit once, the time signal shows multiple hits in 0.25 [s]. In Figure 5.5, a close-up of the input signal is presented. In addition, the time signal is translated to the frequency domain by using the FFT. Also, the voltage values in the time domain are corrected for the initial offset on the y-axis.

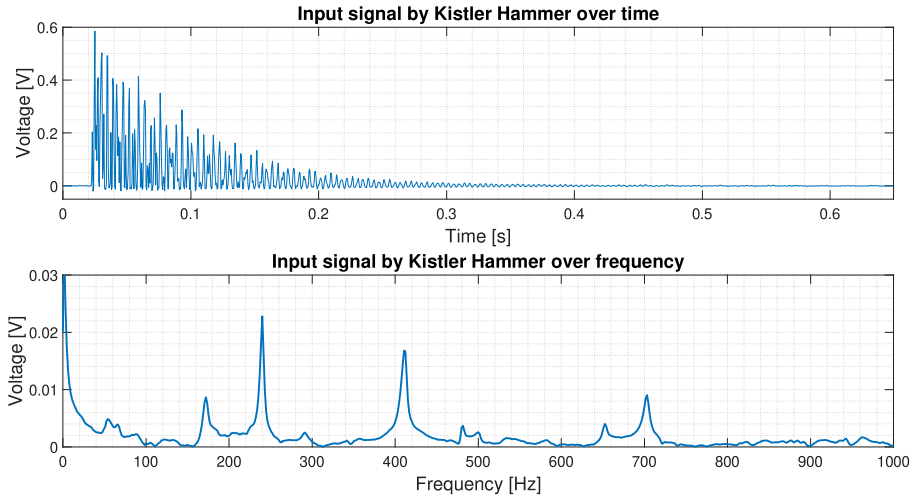

Figure 5.5: Signal inputs in the time and frequency domain.

Multiple impacts are identified in the input signal, which are gradually decreasing in magnitude. This deviates from conventional input signal plots after a single impact[36]. This behavior can be explained by two possible sources: noise or vibration.

Multiple vibrations as input signal

In case the multiple peaks in the input signal represent vibrations, the output signals are significantly influenced. This degrades the quality of the modal analysis [37]. After an assumed single hit on the blade, the multiple peaks indicate reflective impact behavior. This means the blade is vibrating back on the hammer multiple times, imposing a multitude of impacts. As a consequence, the FFT of the input signal is also significantly distorted.

The hammer hit is shortened to reduce the time of contact between the hammer and the blade. However, the gradual decrease in the input signal peaks lasted for at least 0.15 [s]. Industry shows that time of contact is reduced by reducing the mass of the impact hammer and increasing the stiffness of the hammer tip [36]. It is proposed to repeat the impact experiments with a lighter impact hammer and different hammer tips in future studies. This might provide more insight towards the source of distortion in the input signal.

Noise of the input signal

The second possible explanation for the distorted input signal is noise. The noise can be imposed by the sensitivity issues of the impact hammer. The maximum force that the hammer can measure is approximately 5000N. The maximum impact value in the input signal shown in Figure 5.5 is 0.58 [V]. The maximum impact voltage value is translated to Newton[7] with a calibration factor shown in Table 5.1.

[7] The load value can be converted to stress with the area of the hammer tip. This is useful in possible stress-strain curves.

Impact value	0.58	[V]
Calibrated hammer	1.09	[mV/N]
Impact load	536.62	[N]

Table 5.1: Magnitude of impact signal.

The imposed impact is thus using around 10% of the total capacity of the hammer. A higher percentage of the total capacity may reduce the noise in the input signal[8]. Assuming that only the first peak of the input signal is an excitation and the other peaks result from noise, these remaining peaks are removed from the input signal. An artificial design of the input signal is proposed as shown in Figure 5.6.

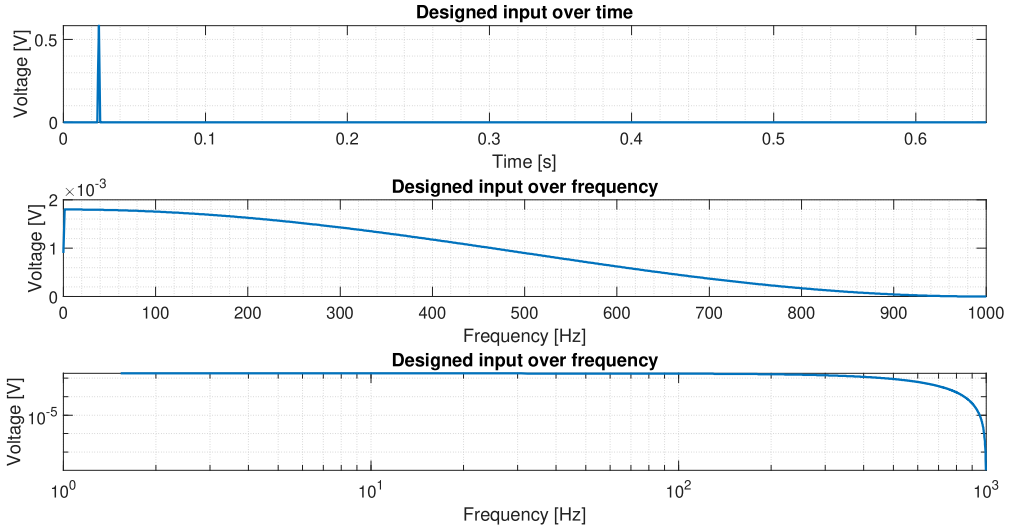

Figure 5.6: Artificial input signal design.

The artificial input is based on the first peak of the original signal in Figure 5.5. Furthermore, Figure 5.6 includes an individual impact load in the time domain, the FFT of the input signal, and the frequency domain in logarithmic scale. The plots are in agreement with conventional time and frequency domains of single impact signals [36].

5.2.2. FRFs of embedded piezoelectric sensors

Since a proposed input signal is designed, the output signals are assessed. For each of the embedded sensors an output signal, similar to the output signal of sensor E5 in Figure 5.4, is obtained. These output signals are a response on the excitation imposed by the impact hammer. This input-output relation is called the FRF. Whereas the response of sensor E5 is previously presented in the time domain, the FRF of this sensor represents the relation between impact load and measured response. The FRF of the embedded piezoelectric sensor E5 related to the original input signal[9] is shown in Figure 5.7.

[8] It is proposed to do the experiments with a hammer with a decreased maximum measurable force. This way, an increased percentage of the maximum capacity of the hammer is established with the same impact load. Also, the lower inertia of the hammer decreases the risk of back-vibration. This is decreased due to the reduced time of contact with the blade.

[9] The input signal prior to removing the other peaks.

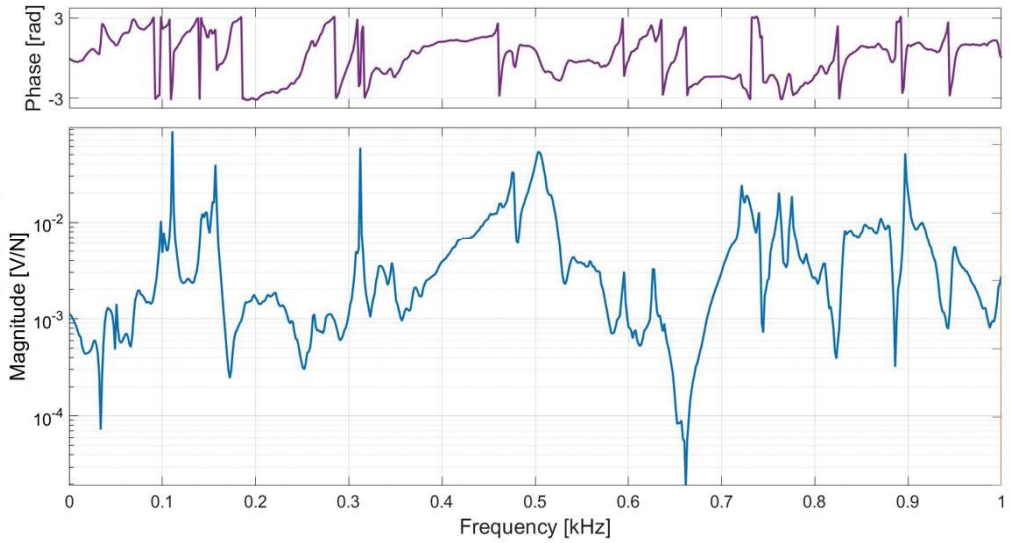

Figure 5.7: Phase & FRF of sensor E5 with original input signal.

The top of the graph shows the phase changes over the frequency domain. At resonance frequencies, phase changes of 2π are expected. However, this is the FRF based on either a multitude of impact loads or noise. It is therefore difficult to determine whether the peaks contribute to the response at a given frequency. In Figure 5.8, a new FRF of the system at sensor E5 is computed. The function is a relation between the designed input signal of the hammer and the measured output by the sensor. It is expressed in displacement[10] [38].

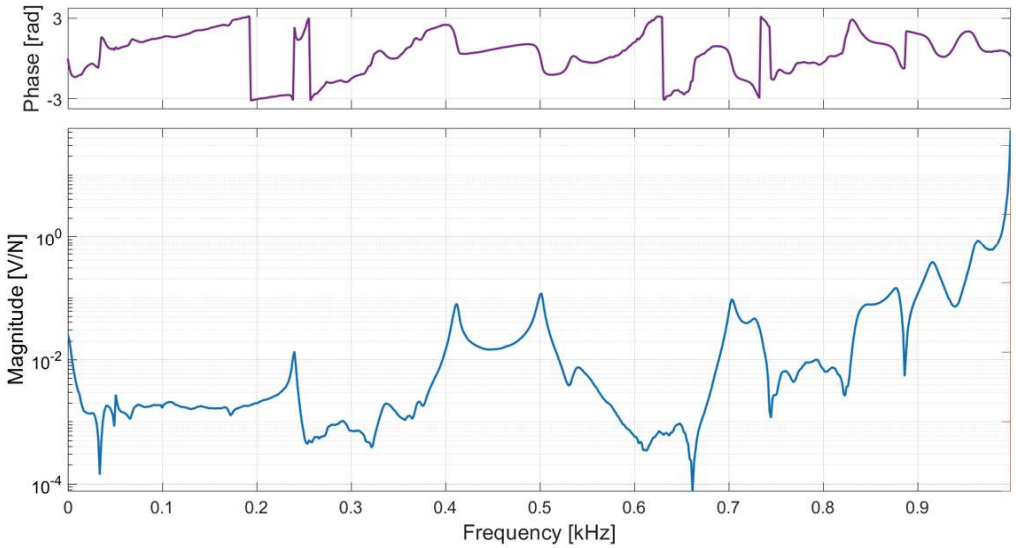

Figure 5.8: Phase & FRF of sensor E5 with the designed input signal.

The magnitudes of the peaks at modal frequencies are presented with an increased distinctness compared to the FRF of the original input signal. It shows that from 700Hz the FRF is more distorted. For higher frequencies, it is possible that the response is less related to the input signal[11] and noise influences the result. Therefore, the FRF is showing less distinctive peaks. The prominent natural frequencies are captured and shown in Table 5.2.

[10] This is convenient since displacement is linearly related to strain in the elastic region.
[11] This correlation of output to the input signal can be quantified with the coherence number.

Mode no.	1	2	3	4	5	6
FE frequency	210	332	483	579	701	818
Measured frequency	240	412	501	703	838	[-]
Increase of FE	14.3%	24.1%	3.7%	21.4%	19.5%	[-]

Table 5.2: Difference in natural frequencies of FEM and measurements from sensor E5.

The measured frequencies by piezoelectric sensor E5 are significantly different from the natural frequencies computed by FEM. However, the focus of this study relates to the mode shape rather than the resonance frequencies. The behavior of the blade at these frequencies is assessed. An agreement should hold between the behavior from measurements and FEM.

From Figure 5.8, the response magnitudes at the natural frequencies are captured for piezoelectric sensor E5. The FRFs of the other embedded sensors are shown as imaginary responses and presented in Section 5.2.3. It must be noted that the magnitudes are computed as voltage values. The voltage measured by the embedded sensor is based on deformation in both translation and rotation directions.

5.2.3. Voltage mode shapes from piezo-sensors

The voltage values of ten embedded piezoelectric sensors in the first five modes are compared to the deformation in the z-direction of the FEM. For this comparison, the FRF is decomposed. The FRF consists of complex numbers which are converted to consecutively phase, real, and imaginary parts. Figure 5.9 shows the decomposition of the FRF measured at embedded piezo-sensor E5.

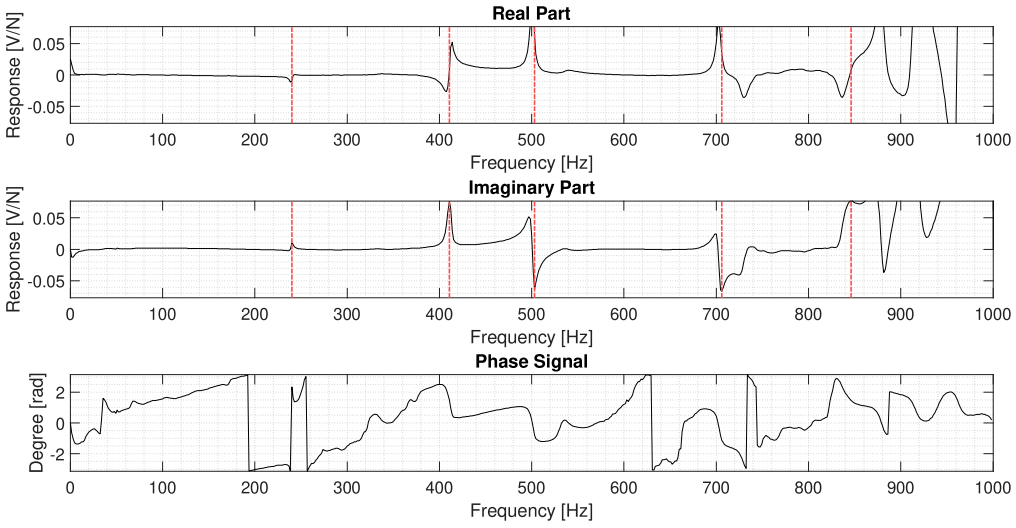

Figure 5.9: Real, imaginary, and phase of piezo-sensor E5.

The real part of the FRF should be zero at resonant- or natural frequencies. Hence, there is zero energy flux across the blade. The valley and peak follow each other closely at the natural frequencies. In the imaginary part of the FRF, either a valley or peak value are expected at natural frequencies. The sign of the local maximum is used in determining the mode shape of the blade. It shows whether the blade is either in compression or tension at the measurement location. This phenomena is absent at 500Hz and 700Hz in the imaginary plot of Figure 5.9. These discrepancies in the imaginary part of the FRF compared to conventional behavior underlies the distortions found in the input signal[12]. The modal voltage values of the nine remaining embedded piezo-sensors are shown in Figures 5.10, 5.11, and 5.12 for computing the mode shapes of the blade.

[12] Although the input signal is re-designed as a single impact load, the succeeding impacts or noise effects are not necessarily removed from the output signals. They might influence the measured output.

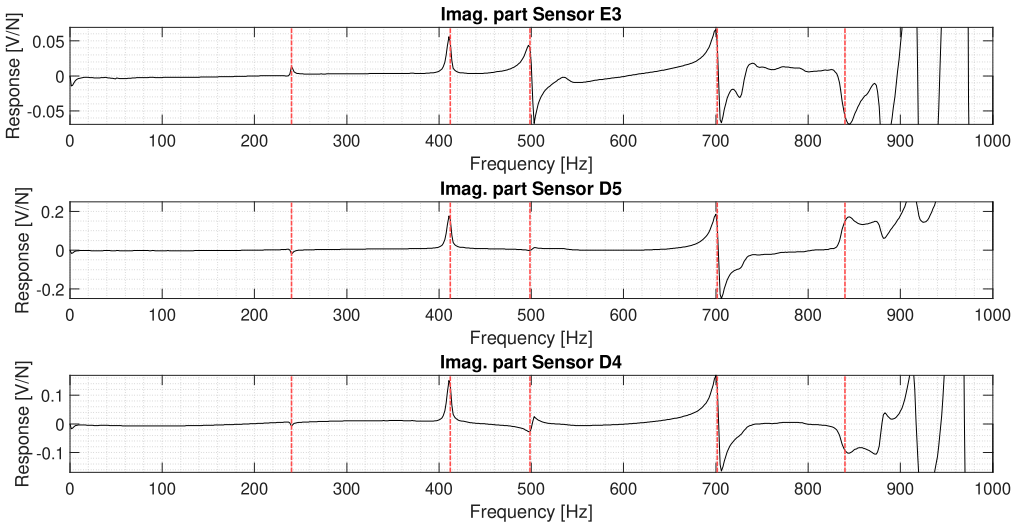

Figure 5.10: Imaginary part of FRFs - Sensors E3, D5, D4.

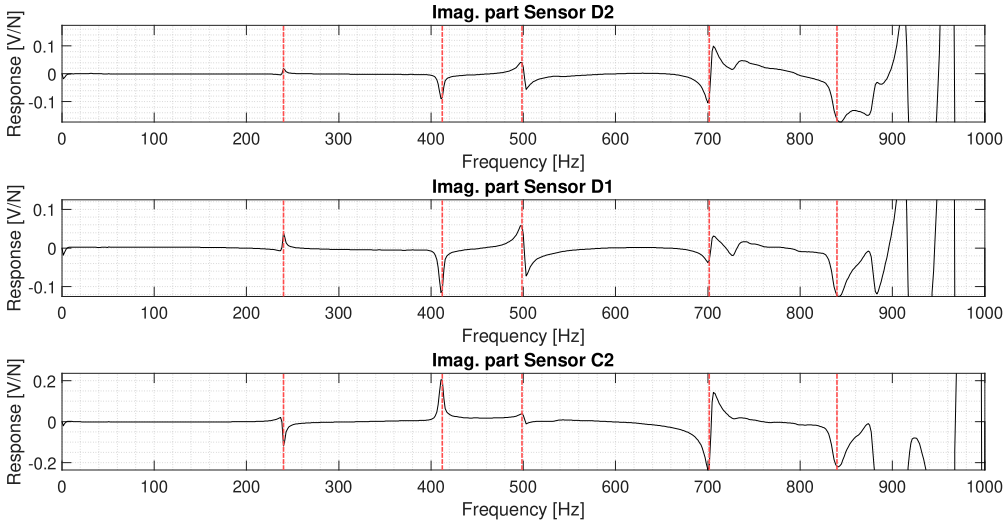

Figure 5.11: Imaginary part of FRFs - Sensors D2, D1, C2.

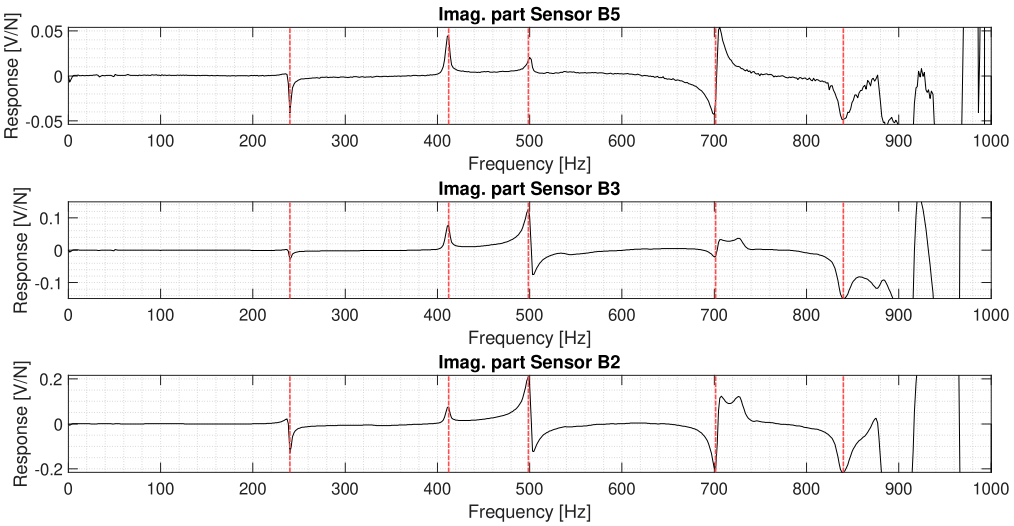

Figure 5.12: Imaginary part of FRFs - Sensors B5, B3, B2.

The responses of the first two modes, the first two peaks in each graph, show promising results with peaks pointing in either positive or negative directions. However, the first mode of the blade is expected to be a bending mode. This assumption would provide a response in which the peaks of the first mode would all point in the same direction[13]. The peaks of the second mode seem to be clean results without much distortion. The third and fourth mode show a sign shift in a short frequency window. It is possible that this shift is caused by two eigenfrequencies of which one has a negative response and the other results in a positive response. Again, a second reason is the possible interference of the distorted input signal on the response output. Understanding the modal responses is important to assess the ability of embedded sensors to obtain dynamic properties. Therefore, further comparison with the FEM is necessary in analysing these modal responses.

[13]The first mode does not show to have the same sign for the response at each measurement location. It needs to be verified which mode shape is related to the first natural frequency.

5.2.4. Voltage mode shape comparison with FEM

In Figure 5.13, the behavior of the blade is visualized for the first mode under strain in z-direction ε_{33}. The coordinate system is provided in the figure. Strains are given in millimeters per meter. For convenience, the locations of the embedded piezo-sensors are captured and added in the figure. Note that the piezo-sensors are embedded in the suction side.

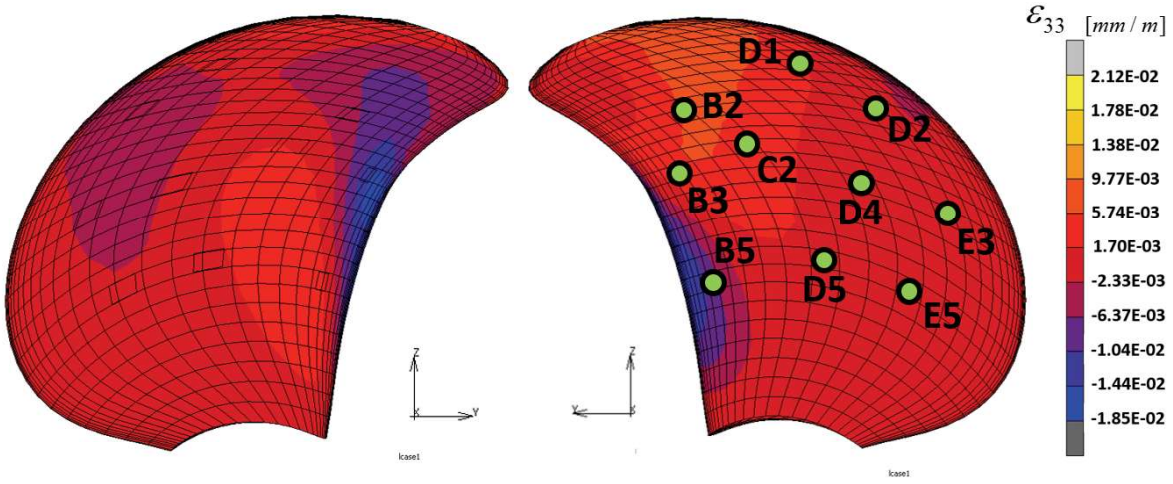

Figure 5.13: Mode shape 1 computed by Marc Mentat - pressure & suction side.

Using the colorbar on the right-hand side of the figure, it shows that the first mode of the blade is mostly in minor tension at the suction side tip of the blade. The trailing edge goes from a tensile to a compressive state in direction of the root. To provide a more convincing analysis of the mode shape, the contributions of other strain components have to be taken into account. The collection of strain components is expressed in a voltage output using the electro-mechanical coupling, explained in Chapter 2. The resulting voltage output is shown in Table 5.3.

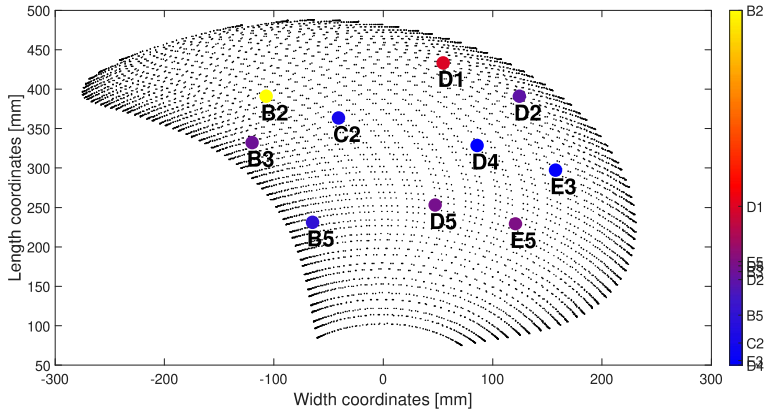

Sensor	Norm. [-]
B2	1
D1	0.31
E5	0.12
D5	0.10
B3	0.08
D2	0.05
B5	-0.07
C2	-0.17
E3	-0.23
D4	-0.25

Table 5.3: normalized voltage of FEM at ten locations - Mode 1.

It is important to assess the agreement of the mode shape visualized by FEM and the one measured by the embedded piezo-sensors. The imaginary part of the FRFs is previously captured and is visualized in Table 5.4. The degree of agreement is assessed with both the colorbar and a table with normalized voltages.

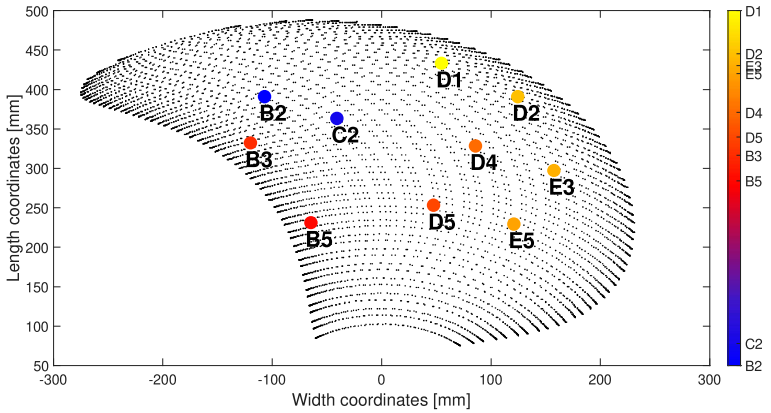

Sensor	Norm. [-]
D1	0.31
D2	0.15
E3	0.11
E5	0.08
D4	-0.07
D5	-0.16
B3	-0.22
B5	-0.32
C2	-0.92
B2	-1

Table 5.4: normalized voltage from embedded piezo-sensors - Mode 1.

First, the locations of the minimum and maximum normalized values are compared. It shows that B2 is the maximum in FEM, but the minimum value in the measurements. The sequence of the normalized values of FEM location exhibits limited agreement with the sequence computed by the sensor measurements. However, the signs of the normalized values provide important additional information. It proclaims that the blade is either in tension or compression at that particular location in the specific mode. Sign-agreement is found in 70% of the table. Sensor locations B2, B3 and E3 are not in agreement. A correlation between the location on the blade surface and the discrepancies are unfounded for results of Mode 1. The comparison results of Modes 2, 3, 4 & 5 are shown in Table 5.9.

	FEM		**Meas.**
Sensor	Norm. [-]	Sensor	Norm. [-]
B3	0.09	C2	1
D1	-0.22	D5	0.85
D2	-0.22	D4	0.73
E5	-0.26	E5	0.37
E3	-0.27	B3	0.37
D5	-0.47	B2	0.37
B2	-0.57	E3	0.27
D4	-0.81	B5	0.21
B5	-0.90	D2	-0.43
C2	-1	D1	-0.56

Table 5.5: Mode 2

	FEM		**Meas.**
Sensor	Norm. [-]	Sensor	Norm. [-]
D5	0.06	B2	1
E5	0.05	B3	0.60
E3	0.02	C2	0.18
D1	0.00	B5	0.10
B5	-0.01	D5	0.06
D2	-0.01	D4	-0.13
B3	-0.07	D2	-0.27
D4	-0.07	E5	-0.31
C2	-0.11	E3	-0.32
B2	-1	D1	-0.34

Table 5.6: Mode 3

	FEM		**Meas.**
Sensor	Norm. [-]	Sensor	Norm. [-]
B2	0.28	D4	0.68
E3	0.08	B5	0.22
D4	0.04	B3	0.13
B5	0.02	D1	-0.15
D2	-0.06	E5	-0.27
D1	-0.14	E3	-0.27
E5	-0.21	D2	-0.42
D5	-0.33	B2	-0.81
C2	-0.41	C2	-0.95
B3	-1	D5	-1

Table 5.7: Mode 4

	FEM		**Meas.**
Sensor	Norm. [-]	Sensor	Norm. [-]
B2	1	D5	0.78
B5	0.84	E5	0.35
D1	0.16	B5	-0.22
D5	0.09	E3	-0.31
E3	0.05	D4	-0.46
E5	0.00	D1	-0.57
D4	-0.01	B3	-0.68
C2	-0.12	D2	-0.79
D2	-0.14	B2	-0.98
B3	-0.26	C2	-1

Table 5.8: Mode 5

Table 5.9: Comparisons of normalized values - Mode 2, 3, 4 & 5.

The graphical results from Table 5.9 are found in Appendix C. In Mode 2, 70% of the values obtained through measurements have an opposite sign. Where Mode 1 showed potential agreement, Mode 2 differs from this trend. It is possible that the second mode shape of FEM corresponds predominantly with another mode determined from measurements. Hence, the FEM values of Table 5.7 are compared with the piezo-sensor values from the table in Figure 5.4. Analysis of the lower half of both tables shows that the leading edge values D1, D2, E3, and E5 correspond to certain extent by namely the colorbar. However, their signs do not match. Therefore, it is premature to conclude a level of agreement of these two different modes from different methods.

Further assessment of the results in Table 5.9 and Appendix C shows that minor correlation exists between other modes as well. The computed normalized values by the methods are studied to find the cause of these differences. For FEM, the strain components of an element are extracted at the layer that corresponds with the real layer in which the piezo-sensor is embedded. The size of this element-layer is larger than the size of the piezo-sensor. Minor differences can originate from this discrepancy between the two methods although sign differences within an element are only expected at nodal lines or points[14]. For the embedded piezo-sensors, defaults are possible to originate from soldering the sensors up to the measurement system.

In order to exclude the FEM of causing the non-corresponding mode shapes, a comparison is set up between surface-mounted strain gauges and the FEM. The strain gauges are placed in the z-direction of the blade. The z-direction is previously shown in the coordinate system of Figure 5.13.

5.3. Results of Serie A strain gauges

This section includes the responses in the time and frequency domain of the blade mounted strain gauges of Serie A and their corresponding embedded piezoelectric sensors[15]:B_3, B_2, D_1, D_2, and D_4.

5.3.1. FRF output signal of Serie A

The signal response data is presented in the frequency domain as a function of volts over force. It shows which frequencies are dominant in the response after excitation. Figure 5.14 shows the FRF of blade mounted strain gauge B3, including the phase over the frequency domain.

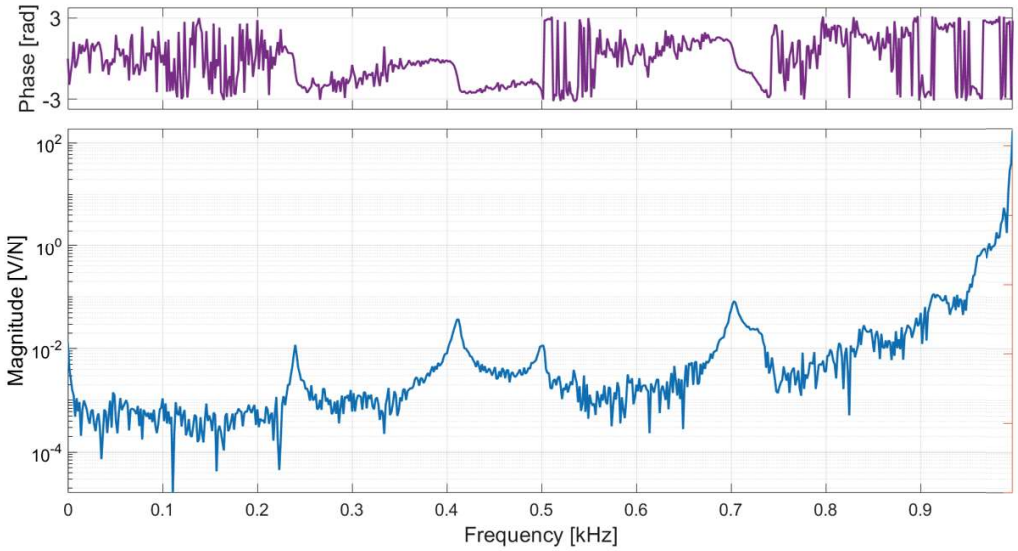

Figure 5.14: FRF of strain gauge B3 with designed input signal.

[14]Nodal lines or points are positions on the blade that have a net-zero deformation in one or more mode shape(s).

[15]The remaining piezoelectric sensors are monitored as well, but can not be compared to an external measuring method. Therefore, these results are not discussed in this section.

Similar to the FRFs of the embedded piezo-sensors, the graph shows the measured strain gauge response relative to the input signal. Again, the response increases exponentially after 750Hz. The accuracy of measured resonance peaks below this frequency are assumed to be useful in analysis. The five identified resonance peaks of the strain gauges correspond to the frequencies shown in Table 5.2. Compared to Figure 5.8, the FRF of the strain gauge contains a lot more noise. This observation also holds for the phase. Since both sensing methods are connected to the DAQ system, it is possibly caused by the amplifier. Additionally, application effects have to be taken into account. One sensing method is positioned within the blade while the other measures on the blade surface. Once again, the FRF is decomposed, see Figure 5.14.

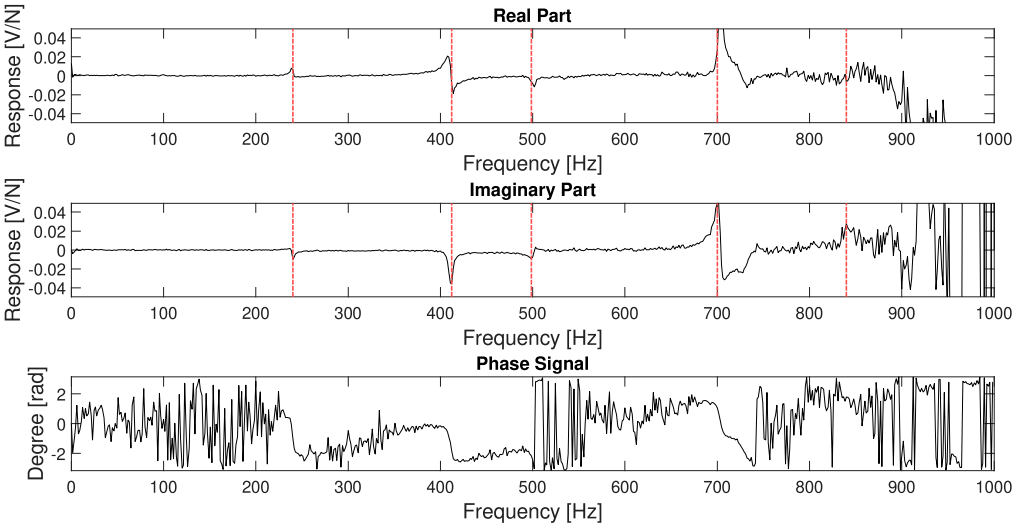

Figure 5.15: Decomposition of FRF - Strain Gauge B3.

The real and imaginary parts are distinguished together with the phase, the latter also being provided in Figure 5.15. The first five natural frequencies found are subsequently at 240Hz, 412Hz, 501Hz, 703Hz, and 838Hz. These frequency values are in agreement with the natural frequencies measured by the piezo-sensors. The values of these peak frequencies in the imaginary parts are used to determine the mode shape of the blade. The imaginary responses of strain gauge locations B2, D1, D2, and D4 are shown in Figure 5.16.

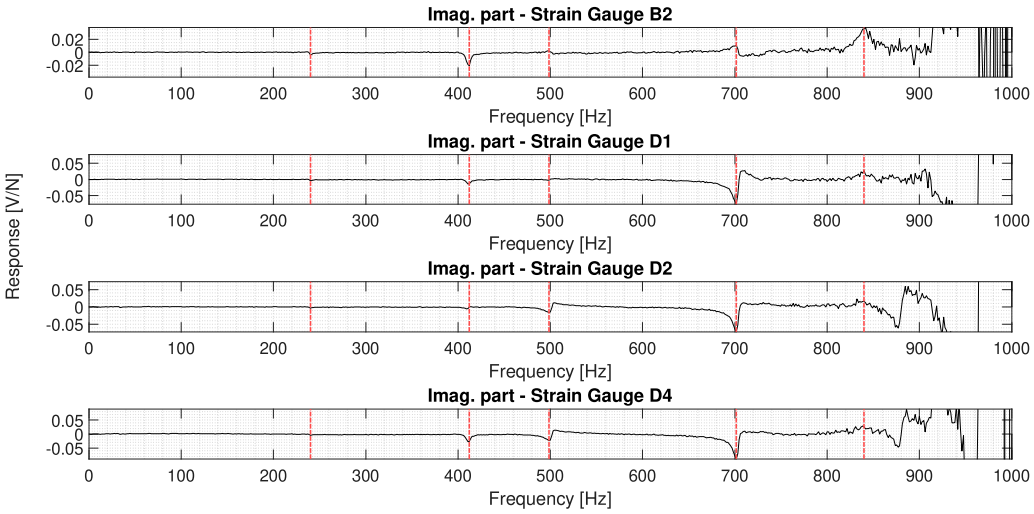

Figure 5.16: Imaginary parts of strain gauges B2, D1, D2, D4.

In general, the measurements of natural frequencies of both the embedded piezo-sensors and the blade mounted strain gauges show to be in agreement. It is noted that the minima and maxima in the response after 750Hz contain more noise. However, the resonance frequency of 838Hz is included in the mode shape comparison.

Since the strain gauges measure in a single direction, it is more convenient to compare the measured values by these gauges with FEM than directly with the embedded piezo-sensors. Namely, FEM is also able to provide values in a single direction. To substantiate this second comparison, the imaginary response of strain gauge B3 in Figure 5.15 is compared with the result of piezo-sensor B3 in Figure 5.12. The response of strain gauge B3 has different signs for several modes. Therefore, it is assessed whether the strain gauges are in better accordance with FEM than the embedded piezo-sensors are with FEM.

5.3.2. Mode shape visualisation with Serie A results

The mode shape values of the third strain component at the five strain gauge locations are visualized in a top view of the blade. Figure 5.17 shows the response for the first mode detected by FEM. The strain magnitude is provided with a color chart. Strain gauges that are included in Serie A are indicated in as green dots while inactive strain gauges are light-grey.

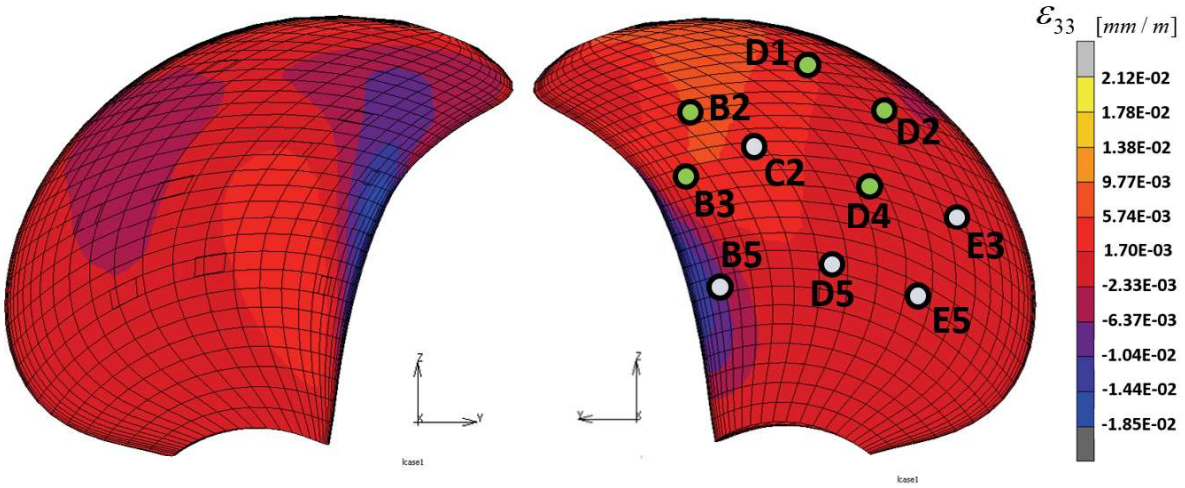

Figure 5.17: Mode shape 1 computed by Marc Mentat - pressure & suction side.

In Figure 5.10, the active strain gauges are shown together with their normalized strain values. It appears that D4 has the highest negative strain in strain gauge measurements whereas in FEM this does not hold. The locations in FEM show predominantly positive strain values.

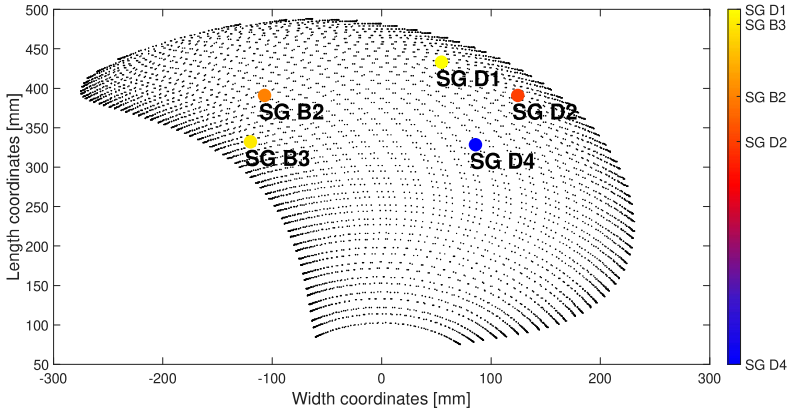

Sensor	Norm. [-]
D1	-0.38
B3	-0.41
B2	-0.53
D2	-0.61
D4	-1

Table 5.10: Strain in z-direction for mode shape 1 measured by strain gauges - pressure & suction side.

The results of the strain gauge values for the remaining modes are found in Appendix D. The measured normalized strain for the second mode shows minor agreement with the second mode in FEM. These strain gauge values of the second mode also lack correspondence with the other mode shapes computed by FEM. A modal assurance criterion (MAC) is used in order to evaluate the level of agreement between mode shapes from FEM and the strain gauges.

5.3.3. MAC matrix of FEM and strain gauge data

The MAC is a statistical indicator that is most sensitive to large differences in mode shapes. It must be noted that the MAC matrix indicates consistency but not necessarily validity or orthogonality[16]. The modal values of the strain gauges from Figure 5.10 and Appendix D are isolated for the first five modes. Hence, a [5×5] matrix is obtained with strain gauge values. An equal sized matrix with FEM results is used in the comparison. The criterion is computed using the two matrices in Equation 5.2. The results of the MAC function are shown in Figure 5.18a & 5.18b.

[16] The MAC does not prove that one mode shape cannot be constructed by a linear combination of any other mode shape.

$$\text{MAC}\left(\{\varphi_{sg}\},\{\varphi_{fem}\}\right) = \frac{\left|\{\varphi_{sg}\}^T\{\varphi_{fem}\}\right|^2}{\left(\{\varphi_{sg}\}^T\{\varphi_{sg}\}\right)\left(\{\varphi_{fem}\}^T\{\varphi_{fem}\}\right)} \tag{5.2}$$

φ_{sg} =	Modal vector of strain values - strain gauges
φ_{fem} =	Modal vector of strain values - FEM

Table 5.11: Definitions of MAC variables.

For each position in the MAC matrix, a criterion is computed based on the modal vectors of both measuring methods. Hence, position $\{1,1\}$ in Figure 5.18a is based on the modal strain values of mode 1 measured by the strain gauges and the modal strain values of Mode 1 computed from FEM. Position $\{1,2\}$ is computed with the same strain gauge values of Mode 1, but with the modal strain values of Mode 2 extracted from FEM. In total, Equation 5.2 is used 25 times to construct Figure 5.18a.

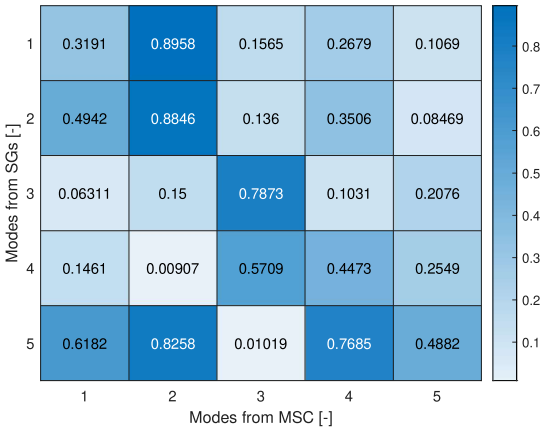

(a) Consistency criterion mapping.

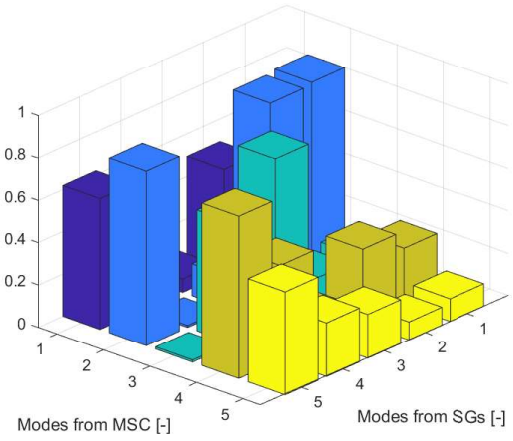

(b) 3D representation of MAC matrix.

Figure 5.18: Results of MAC for Serie A and FEM .

In the assessment of the consistency of the MAC-matrix, the graphical representation of the modes from Appendix D are used[17]. The first two modes shapes measured by the strain gauges show to be similar with different magnitudes. Therefore, it makes sense that the first and second modes from the strain gauges both correspond to the second mode shape of FEM. The suction side in FEM shows to be predominantly in tensile strain. However, a higher indicator is expected for the first FEM mode shape as well[18]. Furthermore, the fifth mode measured by the strain gauges shows to correspond with multiple modes from FEM. Discrepancies for higher modes in a MAC analysis might be related to higher frequencies. These frequencies tend to have relative low response amplitudes. Also, computing a MAC matrix for more modes than available measuring points is considered to decrease the accuracy of measuring consistency in the mode shapes[19].

Based on the results, inconsistencies are found between the FEM and both measuring methods: embedded piezo-sensors and blade mounted strain gauges. Conclusions related to the results are found in Chapter 6. Recommendations and discussion on further research on the agreement of FEM and measurements are found in Chapter 7.

[17] This appendix contains the strain component ε_{33}.
[18] Lower modes often show a relative high response and are therefore expected to be measured more accurately.
[19] A mode shape that has three nodal points cannot be accurately measured by two measurement points [39].

6

Conclusion

For answering the research question as stated at the start of the thesis study:

> *How can the dynamic response of an FRC propeller be reconstructed by using embedded piezoelectric sensor measurements?*

Conclusions are described in this chapter regarding the subquestions.

6.1. Modeling full-field strain

> *How can full-field strain be reconstructed based on a network of embedded sensors?*

The modal properties of the FRFs of a limited amount of embedded piezoelectric sensors are obtained from excitation with an impact hammer. Mode shape values and voltage data of the reduced system can be computed to obtain the principal coordinate vector of the vibrations. Full-field strain reconstruction of a flexible propeller is possible when blade FEM and experimental data are in accordance.

> *How can a finite element model of the blade be used in the analytic method of full-field strain reconstruction?*

The FEM of the blade is used for constructing the reduced modal matrix with the mode shape values. Their coordinates correspond approximately with the locations in the actual blade where the piezoelectric sensors are embedded.

6.2. Design of sensor embedment

> *How can a distributed network of piezoelectric sensors be embedded in an FRC marine propeller blade?*

The fabrication of a composite marine propeller blade with dry fibers enables the ability to embed multiple sensors individually. Embedding an individual sensor is possible for any preferred layer in the laminate. Wiring of the intact sensor circuits is capable of transferring sensor response. The survival rate of the wiring is uncorrelated to the survival rate of embedded sensors.

> *How can the embedded sensors be localized and identified?*

Computerized tomography is used for the localization of the embedded sensors. Notable translational movement of the sensors during fabrication is not detected from the resulting scan. The identification of the individual circuits to the corresponding embedded sensors is deemed sufficient by applying pressure manually. Manual pressure should not be used in excitation measurements because of the risk of thermal effects.

6.3. Experimental procedure

How are dynamic properties of an FRC blade obtained by an embedded sensor network?

Each sensor system is connected to a DAQ system via a breadboard. The DAQ features enable the representation of the response of each piezoelectric sensor. The dynamic responses are obtained in Volts in both the time and frequency domain. The input signal imposed by an impact hammer is captured in Newtons. With the impact hammer used in this study, it is assumed that only the first peak in the input signal imposes a mechanical vibration. For the sake of post-processing, the remaining peaks of the input signal are considered to be either noise or non-contributing vibrations.

The relation between the input- and output signal, the FRF, is captured for each intact sensor at specific locations. Dynamic properties such as the natural frequencies of the blade are captured with these FRFs. The response values at natural frequencies in the FRFs are used to obtain the mode shapes of the blade. Directional components of dynamic properties are not obtained from these domains.

Surface-mounted strain gauges might obtain the directional components in experiments. The strain gauge results are expressed in either strain or voltage. Also, a full Wheatstone bridge is used to compensate for temperature differences between measurements[1]. The strain gauge results are used in comparison with FEM results.

6.4. Comparison of model with experimental results

How do the dynamic measurements by the embedded sensor network compare to both the strain gauges and finite element model?

The dynamic measurements of an individual sensor are executed simultaneously with their corresponding surface-mounted strain gauges of Serie A in an impact hammer experiment. The FRFs of the strain gauges and embedded piezoelectric sensors agree in terms of computed natural frequencies. This holds for the first four natural frequencies between 1Hz and 730Hz.

The modal values from the FRFs of 10 intact piezo-sensors are expressed as normalized voltage vectors for each mode. The directional modal strain components of the corresponding locations in FEM are also computed as a normalized voltage vector, following the electro-mechanical coupling theory. Results show that both methods' normalized modal voltage vectors are in insufficient agreement. It is concluded that there are five possibilities for this disagreement: the use of incorrect boundary conditions in FEM, errors in the analytical application of the electro-mechanical coupling, discrepancies in the voltage measurements by the embedded piezo-sensors, fabrication inconsistencies compared to the FEM, and/or an incorrect response of the blade due to the impact hammer properties[2].

Using the results of the strain gauges FRFs makes it possible to bypass the use of the electro-mechanical coupling as described in Chapter 2. Instead, a more straightforward coupling term is computed with the strain gauge amplifier. Five strain gauges (Serie A) are used to compute UD modal strain vectors. These vectors are used to compare the modal strain vectors from corresponding locations in FEM in a MAC matrix.

[1] The significance of the full Wheatstone is not studied in this research.
[2] The properties include the inertia of the hammer and stiffness of the tip.

The resulting MAC matrix indicates discrepancies between the strain gauges and FEM values. Since this second comparison also lacks agreement, it is concluded that inconsistencies exist between the FEM and the actual blade. Incorrect voltage measurements by the embedded piezo-sensors are less likely since the resulting FRFs of the strain gauges and piezo-sensors showed similar natural frequencies. It is concluded that the future study must focus on corresponding material properties and boundary conditions of FEM and the actual blade. This could improve the consistency of measurement locations and eventually allow for a full-field dynamic response reconstruction of an FRC propeller blade.

7

Discussion & Recommendations

This chapter discusses the executed study and includes recommendations for future research.

7.1. Blade fabrication

Blade fabrication involved plies that had non-corresponding fiber directions regarding the plies used in FEM. It is strongly advised to have improved agreement between the real ply cutting plan and the FEM. The cutting plan is not adjusted in this fabrication since previous research fabricated the same FRC blade - without embedded piezoelectric sensors [2]. It was expected that the previous research used the same cutting plan. That research showed good agreement between the natural frequencies found by experiments and the FEM.

The fabrication of the first blade with embedded piezoelectric sensors involved a vacuum-supported RTM process. During this process, the entire mould is packed within a vacuum bag. All components of the blade and sensor systems are in the mould except for the coaxial cables. However, the resin transferred through the mould can flow between the mould and the enclosing vacuum bag. The coaxial cables must be protected from resin. A safety bag, secured with tacky tape, was used to protect the cables. For several reasons, resin did compromise the safety bag. At the end of each wire, the SMA connectors were contaminated with cured resin. Furthermore, more than half of the wires fractured while releasing the plug from the blade root. In the fabrication of the second blade, it is suggested to put the wires in a closed non-adhesive Teflon bag inside the mould. In theory, the package of wires can be taken out of the sleeve in the blade root after the curing process.

7.2. Experiments

The experimental setup is expected to influence the outcome of the measurements significantly. A metal chain is used as a single-point suspension for the blade in the experimental setup. This does not make the blade a totally free-floating object. In future free vibration tests of the blade, the boundary condition at the root can be adjusted. The stiffness of the suspension can be decreased to allow for more vertical translation of the blade. This better represents the free conditions at the root than the metal chain. Clamping the blade at the root is also an option. Since the clamped boundary condition is previously used in experiments [2], the results of future studies using this boundary condition allow for a more convenient comparison.

As mentioned, future study plans the fabrication of a second blade. Assuming an increased sensor system survival rate using the Teflon bag, the resolution of the mode shapes is expected to increase due to more output measurements. In addition, the results from the gauges and embedded sensors can be compared with the results from the current study.

The strain gauges are connected to a full Wheatstone bridge in this study. No experiments are performed without using the Wheatstone bridge. It could be interesting to study the significance of the (full)

Wheatstone bridge on the outcome of strain data. Additionally, the rosette is applied on a substitute FRC specimen. However, the material properties are not compared to the properties of the FRC blade. It is therefore uncertain to assume the full Wheatstone is correcting for thermal differences correctly. A more convenient solution for successive research is to use the fabricated blade of this thesis as the substitute FRC specimen. This solution can provide the second FRC blade with embedded piezoelectric sensors with an undisputed full Wheatstone bridge.

7.3. Modeling

It is concluded that significant differences exist in the modal values of the FEM and both measuring methods used in this thesis. Therefore, the selected locations in FEM and the measuring locations on the real blade used to compute the modal values are discussed. The selection locations from FEM are approximated from a 2D map of the designed sensor layout. The FEM locations should already be based on the actual embedded sensor locations in future research. It possibly improves modal values between FEM and measurement.

Furthermore, the proposed model uses a one-way coupling from strain to voltage. Two-way coupling should be assessed in order to compare these coupling effects. It is possible in FEM to apply this two-way coupling effect. Therefore, future work can implement this effect and update the strain modal matrix.

Lastly, it is expected that boundary conditions and properties of the actual blade are not in agreement with those in FEM. It is concluded that changing these conditions in FEM should be prioritized over fabricating new blades. The blade root sleeve present in the actual blade should be modeled in FEM. Further analysis must be performed on modeling the single-point suspension in FEM. Also, it is found that the material properties provided by manufacturers can deviate up to even 10% [40]. This can also be taken into account when assessing measured natural frequencies of the blade compared to FEM.

7.4. Application

This thesis provides practical insight into applying an embedded network of piezoelectric sensors in an FRC marine propeller blade. Obtaining certain dynamic properties with an embedded network of piezo-sensors is found feasible. Follow-up research can be supported with better knowledge of the FRC propeller blade fabrication. The analytical method should be further developed to enhance the strain reconstruction with reduced input signals. Additionally, underwater excitation testing is the next step in studying blade response using embedded sensors. Future research should also extend to hydrodynamic load measurements and lifetime assessment of the blade.

8

Contribution

The contribution of this thesis is a full-scale application of dynamic response reconstruction of a fiber reinforced composite marine propeller blade. The reconstruction is based on a limited amount of piezoelectric sensors embedded in the composite. The thesis combines studies that involved the full-scale application of dynamic response reconstruction and studies that assessed the influence of sensor embedment in composites. This research succeeds previous research on the marine propeller blade in which an external optical measurement method was used.

References

[1] N. L. Mulcahy, B. G. Prusty, and C. P. Gardiner, "Flexible composite hydrofoils and propeller blades," *Transactions of the Royal Institution of Naval Architects Part B: International Journal of Small Craft Technology*, vol. 153, 1 Jan. 2011, ISSN: 17400694. DOI: 10.3940/rina.ijsct.2011.b1.109.

[2] P. Maljaars, "Hydro-elastic analysis of flexible marine propellers," 2019. DOI: 10.4233/uuid:19c9610b-9a72-42a6-8340-2ba01ec78cc6. [Online]. Available: https://doi.org/10.4233/uuid:19c9610b-9a72-42a6-8340-2ba01ec78cc6.

[3] M. Seaver, S. T. Trickey, and J. M. Nichols, "Strain measurements from fbgs embedded in rotating composite propeller blades," 2006.

[4] V. Giurgiutiu, "Structural health monitoring with piezoelectric wafer active sensors – predictive modeling and simulation," *INCAS BULLETIN*, vol. 2, pp. 31–44, 3 Sep. 2010, ISSN: 20668201. DOI: 10.13111/2066-8201.2010.2.3.4. [Online]. Available: http://bulletin.incas.ro/files/victor_giurgiutiu_v2no3_full.pdf.

[5] M. Mieloszyk, K. Majewska, and W. Ostachowicz, "Application of embedded fibre bragg grating sensors for structural health monitoring of complex composite structures for marine applications," *Marine Structures*, vol. 76, Mar. 2021, ISSN: 09518339. DOI: 10.1016/j.marstruc.2020.102903.

[6] S. Mall, S. B. Dosedel, and M. W. Holl, "The performance of graphite-epoxy composite with embedded optical fibers under compression," *Smart Materials and Structures*, vol. 5, pp. 209–215, 2 1996. DOI: 10.1088/0964-1726/5/2/009.

[7] S. Javdani, M. Fabian, J. S. Carlton, T. Sun, and K. T. Grattan, "Underwater free-vibration analysis of full-scale marine propeller using a fiber bragg grating-based sensor system," *IEEE Sensors Journal*, vol. 16, pp. 946–953, 4 Feb. 2016, ISSN: 1530437X. DOI: 10.1109/JSEN.2015.2490478.

[8] J. Tian, P. Croaker, Z. Zhang, and H. Hua, "Dynamic strain measurements of marine propellers under non-uniform inflow," vol. 744, Institute of Physics Publishing, Oct. 2016. DOI: 10.1088/1742-6596/744/1/012094.

[9] V. E. Zetterlind, S. E. Watkins, and M. W. Spoltman, "Fatigue testing of a composite propeller blade using fiber-optic strain sensors," *IEEE Sensors Journal*, vol. 3, pp. 393–399, 4 Aug. 2003, ISSN: 1530437X. DOI: 10.1109/JSEN.2003.815795.

[10] B. Lin and V. Giurgiutiu, "Modeling and testing of pzt and pvdf piezoelectric wafer active sensors," *Smart Materials and Structures*, vol. 15, pp. 1085–1093, 4 Aug. 2006, ISSN: 09641726. DOI: 10.1088/0964-1726/15/4/022.

[11] S. Shin, B. Zamorano, and N. Elvin, "Comparison of the electromechanical properties of embedded and surface-mounted piezoelectric transducers," *Journal of Intelligent Material Systems and Structures*, vol. 27, pp. 2837–2850, 20 2016, ISSN: 15308138. DOI: 10.1177/1045389X16642299.

[12] S. Gopalakrishnan, M. Ruzzene, and S. Hanagud, *Computational Techniques for Structural Health Monitoring*. Springer London, 2011, ISBN: 978-0-85729-283-4. DOI: 10.1007/978-0-85729-284-1. [Online]. Available: http://link.springer.com/10.1007/978-0-85729-284-1.

[13] A. J. Huijer, "Load and damage measurements on fibre-reinforced composites with embedded piezoelectric sensors a feasibility study Ip," 2019. [Online]. Available: http://repository.tudelft.nl/..

[14] S. J. Rupitsch, "Piezoelectric sensors and actuators fundamentals and applications," 2019. [Online]. Available: http://www.springer.com/series/11054.

[15] H. F. Tiersten, "The linear theory of piezoelectricity," Springer, 1969, pp. 33–39. DOI: https://doi.org/10.1007/978-1-4899-6453-3_5.

[16] J. Erhart, P. Půlpán, and M. Pustka, "Piezoelectric ceramic resonators," 2017. [Online]. Available: http://www.springer.com/series/11054.

[17] S. S. Rao, *Mechanical vibrations*. Pearson Education Inc., 2010, p. 1105, ISBN: 9780132128193.

[18] X. Zhang, "Short-term structural performance of self-monitoring composite marine propellers," 2021. DOI: 10.4233/uuid:479b71c1-a006-4d9a-abda-b000a7711899.

[19] I. M. Daniel and O. Ishai, *Engineering mechanics of composite materials*. Oxford University Press, 2006, p. 411, ISBN: 9780195150971.

[20] R. D. Cook, D. S. Malkus, M. E. Plesha, and R. J. Witt, *Concepts and Applications of Finite Element Analysis*. Hoboken, NJ, USA: John Wiley and Sons, Inc., 2007, ISBN: 0470088214.

[21] G. Gautschi, "Piezoelectric sensorics: Force strain pressure acceleration and acoustic emission sensors materials and amplifiers," 2002. DOI: DOI10.1007/978-3-662-04732-3.

[22] M. Lin and F.-K. Chang, "The manufacture of composite structures with a built-in network of piezoceramics," 2001. [Online]. Available: www.elsevier.com/locate/compscitech.

[23] P. Instrumente, "Datasheet - fast availability of specified versions," 2016. [Online]. Available: https://static.piceramic.com/fileadmin/user_upload/physik_instrumente/files/datasheets/disc-Datasheet.pdf.

[24] P. Instrumente, "Piezoelectric ceramic products - curie temperature," 2021. [Online]. Available: https://static.piceramic.com/fileadmin/user_upload/pi_ceramic/files/catalog_CAT/PI_CAT125E_R3_Piezoelectric_Ceramic_Products.pdf.

[25] SICOMIN, "Epoxy system for injection and infusion," 2014. [Online]. Available: https://polymatrix.hu/wp-content/uploads/2018/09/SR-8100_SD_8822_SD-477x_TDS_UK.pdf.

[26] H. J. Lin and J. F. Tsai, "Analysis of underwater free vibrations of a composite propeller blade," *Journal of Reinforced Plastics and Composites*, vol. 27, pp. 447–458, 5 Mar. 2008, ISSN: 07316844. DOI: 10.1177/0731684407082539.

[27] Micro-measurements, "125uwa strain gauge - datasheet," 2021. [Online]. Available: www.vpgsensors.com.

[28] Micro-Measurements, "125ur rosette - datasheet," 2016. [Online]. Available: www.vpgsensors.com.

[29] Vetek, "Analog signal conditioner - datasheet," 2022. [Online]. Available: https://www.vetek.se.

[30] Y. Ou, D. Zhu, H. Zhang, L. Huang, Y. Yao, G. Li, and B. Mobasher, "Mechanical characterization of the tensile properties of glass fiber and its reinforced polymer (gfrp) composite under varying strain rates and temperatures," 2016. DOI: 10.3390/polym8050196. [Online]. Available: www.mdpi.com/journal/polymers.

[31] S. R. Borukati, A. Ramesh, B. D. Prasad, and S. S. Gowda, "Design and characterization of e-glass fiber reinforced composite material with use of sisal fiber," 2018. [Online]. Available: http://www.ijaerd.com/papers/special_papers/ICTIMES022.pdf.

[32] K. I. Corporation, "Force-aif quartz impulse force hammer - datasheet," 2005. [Online]. Available: www.kistler.com.

[33] K. Maes, E. Lourens, K. V. Nimmen, E. Reynders, G. DeRoeck, and G. Lombaert, "Design of sensor networks for instantaneous inversion of modally reduced order models in structural dynamics," 2014. DOI: http://dx.doi.org/10.1016/j.ymssp.2014.07.018.

[34] E. Lourens, C. Papadimitriou, S. Gillijns, E. Reynders, G. DeRoeck, and G. Lombaert, "Joint input-response estimation for structural systems based on reduced-order models and vibration data from a limited number of sensors," 2012. DOI: doi:10.1016/j.ymssp.2012.01.011.

[35] A. G. Siemens, "Ct system for volume scanning," 1993. [Online]. Available: http://www.meditegic.com/wp-content/uploads/pdfs/siemens_volumezoom.pdf.

[36] G. T. GmbH, "Impulse hammer - wavehit," 2021. [Online]. Available: https://www.gfaitech.com/products/structural-dynamics/impact-hammer-wavehit-max.

[37] C. Instruments, "Basics of modal testing and analysis," 2016. [Online]. Available: https://www.crystalinstruments.com/basics-of-modal-testing-and-analysis.

[38] MathWorks, "Frequency-response functions for modal analysis (modalfrf)," 2017. [Online]. Available: https://nl.mathworks.com/help/signal/ref/modalfrf.html.

[39] P. Avitabile, "Experimental modal analysis," 2001. DOI: https://doi.org/10.1002/9781119222989.ch1. [Online]. Available: https://onlinelibrary.wiley.com/doi/10.1002/9781119222989.ch1.

[40] A. Zaal, "Feasibility evaluation of a non-destructive estimation of material properties of frc structures using ultrasonic guided waves," 2021. [Online]. Available: http://resolver.tudelft.nl/uuid:f72b76d8-6473-4171-bcf8-ecd118c0c70a.

A

Stacking Sequence

LAMINAATOPBOUW Sensorprop Versie 16-06-2021 - V6

Laag	Offset	Zone 1 / Zone 6	Zone 2 / Zone 7	Zone 3 / Zone 8	Zone 4 / Zone 9	Zone 5 / Zone 10	Root 1 / Root 2	Type	Dikte
1		Ondermal							
2		0						ERW 200	0,17
3						0		UD 600	0,5
4							0	UD 600	0,5
5							0	G-Flow	0,5
6							0	UD 600	0,5
7	0mm	-20						UD 600	0,5
8							0	UD 600	0,5
9	-15mm	-20						UD 600	0,5
10	-20mm	0						G-Flow	0,5
11							0	UD 600	0,5
12					-20			UD 600	0,5
13	-10mm	15						UD 600	0,5
14					15			UD 600	0,5
15					0			G-Flow	0,5
16	0mm	60						UD 600	0,5
17						60		UD 600	0,5
18	-5mm	105						UD 600	0,5
19			60					UD 600	0,5
20						60		UD 600	0,5
21			0					G-Flow	0,5
22			15					UD 600	0,5
23					15			UD 600	0,5
24				-20				UD 600	0,5
25				0				G-Flow	0,5
26				-20				UD 600	0,5
27					-20			UD 600	0,5
28						0		UD 600	0,5
29	-30mm							Polymat	1-3
30						0		UD 600	0,5
31					-20			UD 600	0,5
32				-20				UD 600	0,5
33				0				G-Flow	0,5
34				-20				UD 600	0,5
35					15			UD 600	0,5
36			15					UD 600	0,5
37			0					G-Flow	0,5
38						60		UD 600	0,5
39			60					UD 600	0,5
40			105					UD 600	0,5
41						-60		UD 600	0,5
42	0mm	60						UD 600	0,5
43					0			G-Flow	0,5
44					15			UD 600	0,5
45	-10mm	15						UD 600	0,5
46					-20			UD 600	0,5
47							0	UD 600	0,5
48	-15mm	-20						UD 600	0,5
49							0	UD 600	0,5
50	-20mm	0						G-Flow	0,5
51	0mm	-20						UD 600	0,5
52							0	UD 600	0,5
53							0	G-Flow	0,5
54							0	UD 600	0,5
55						0		UD 600	0,5
56		0						ERW 200	0,17

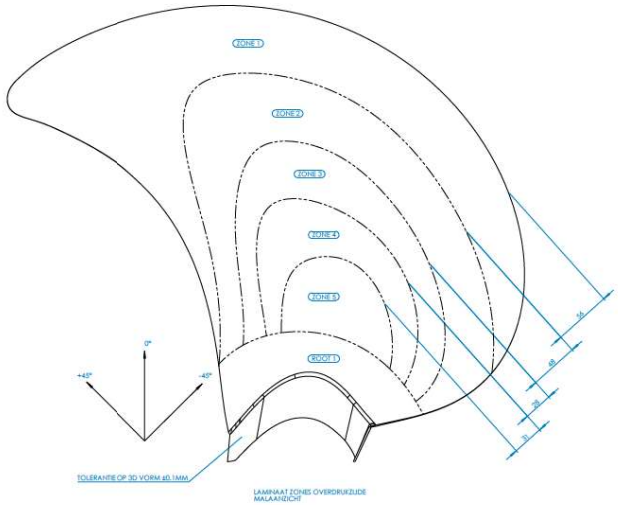

B

Capacitance Measurements

Capacitance Measurements

	Number	Wire	Coax	Difference	Avg. Diff.
Group A	A1	1,179	1,29	9,4%	
	A2	1,163	1,37	17,8%	
	A3	1,173	1,34	14,2%	
	A4	1,181	1,29	9,2%	
	A5	1,159	1,58	36,3%	17,4%
Group B	B1	1,165	1,24	6,4%	
	B2	1,107	1,18	6,6%	
	B3	1,131	1,19	5,2%	
	B4	1,139	1,2	5,4%	
	B5	1,222	1,3	6,4%	6,0%
Group C	C1	1,141	1,25	9,6%	
	C2	1,11	1,26	13,5%	
	C3	1,155	1,21	4,8%	
	C4	1,187	1,28	7,8%	8,9%
Group D	D1	1,133	1,3	14,7%	
	D2	1,164	1,28	10,0%	
	D3	1,141	1,27	11,3%	
	D4	1,185	1,37	15,6%	
	D5	1,225	1,25	2,0%	10,7%
Group E	E1	1,14	1,28	12,3%	
	E2	1,175	1,36	15,7%	
	E3	1,184	1,48	25,0%	
	E4	1,195	1,29	7,9%	
	E5	1,168	1,16	-0,7%	12,1%

C

Modal Voltage Values - FEM & Piezo-sensors

C.1. Mode 1 - 210 [Hz]

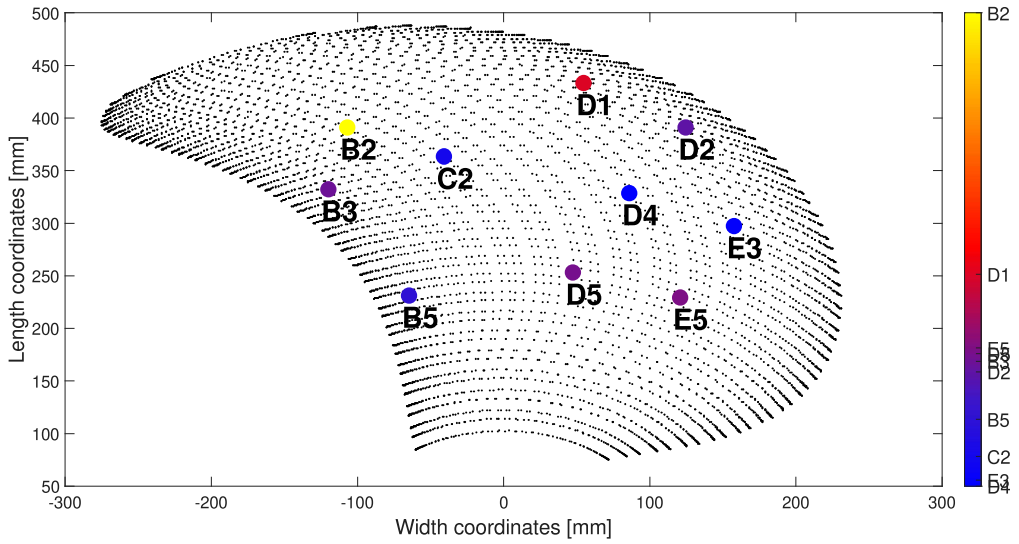

Figure C.1: Mode shape computed by Marc Mentat - Mode 1.

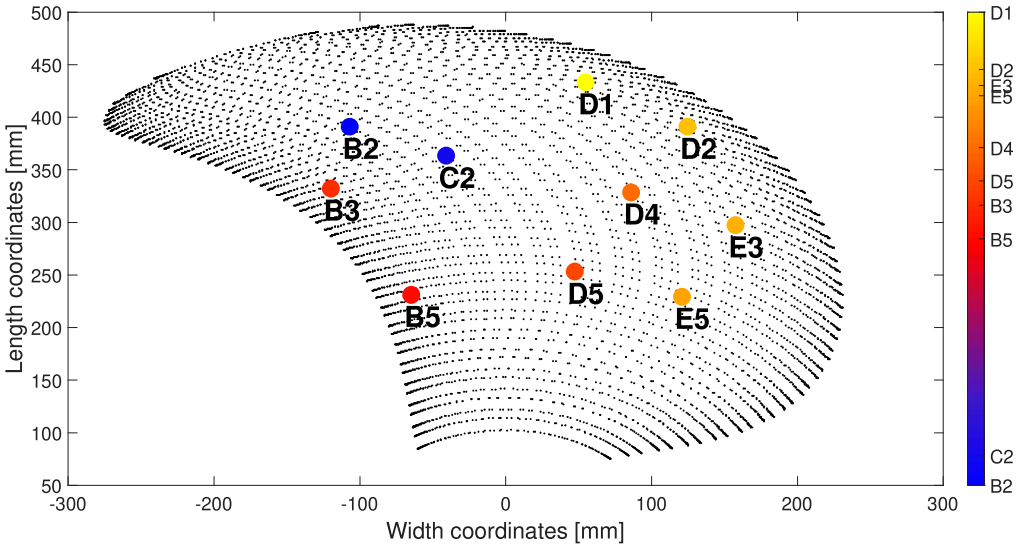

Figure C.2: Mode shape at embedded piezo-sensors - Mode 1.

C.2. Mode 2 - 332 [Hz]

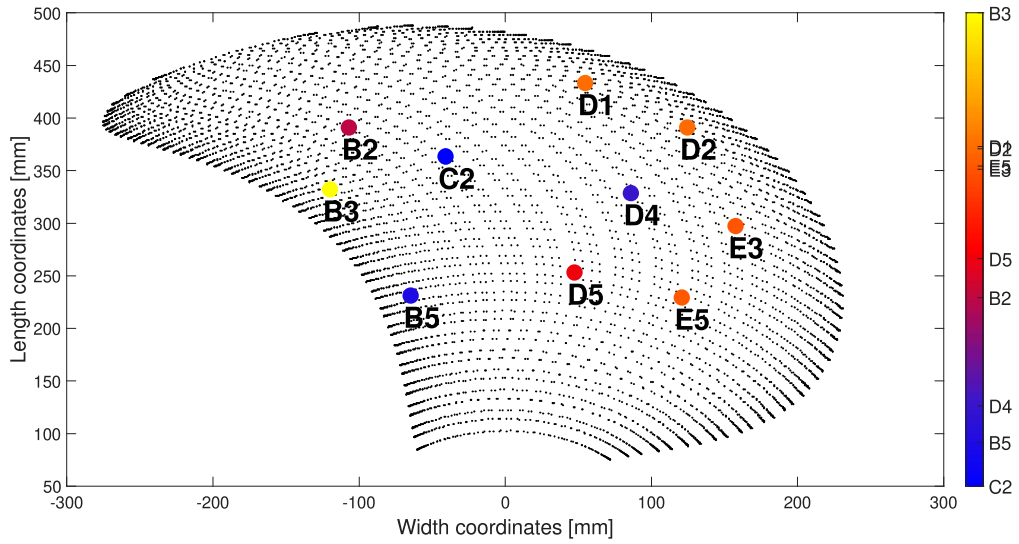

Figure C.3: Mode shape computed by Marc Mentat - Mode 2.

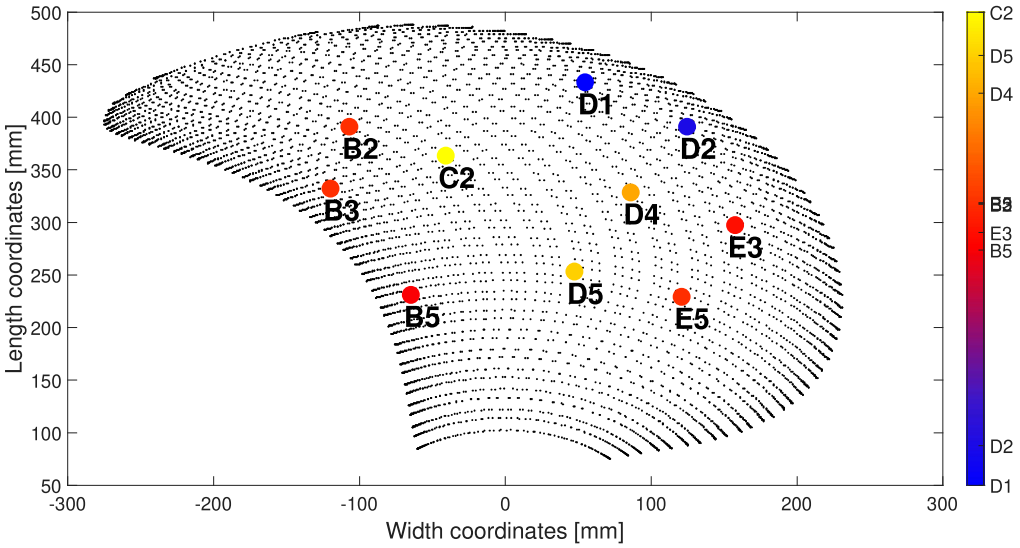

Figure C.4: Mode shape values at embedded piezo-sensors - Mode 2.

C.3. Mode 3 - 483 [Hz]

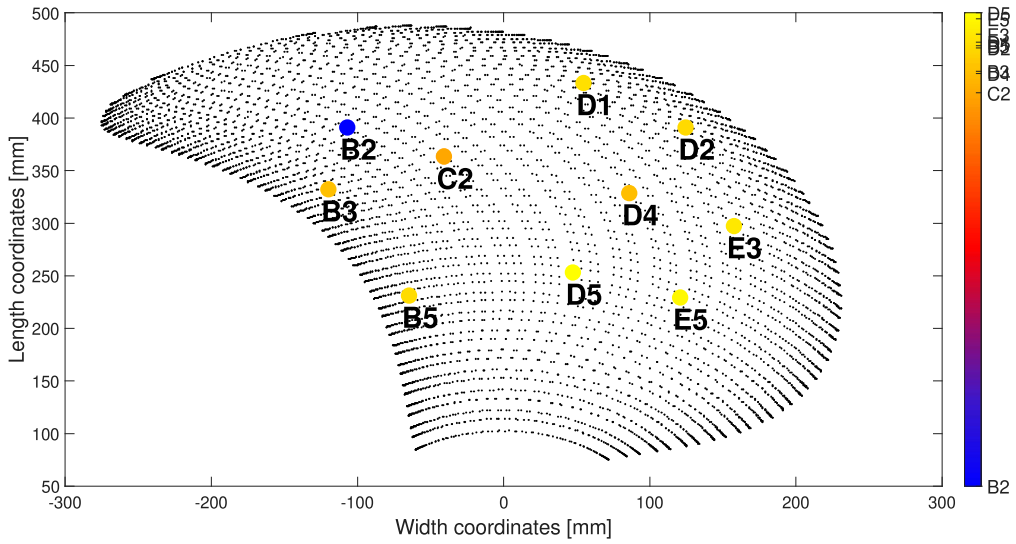

Figure C.5: Mode shape computed by Marc Mentat - Mode 3.

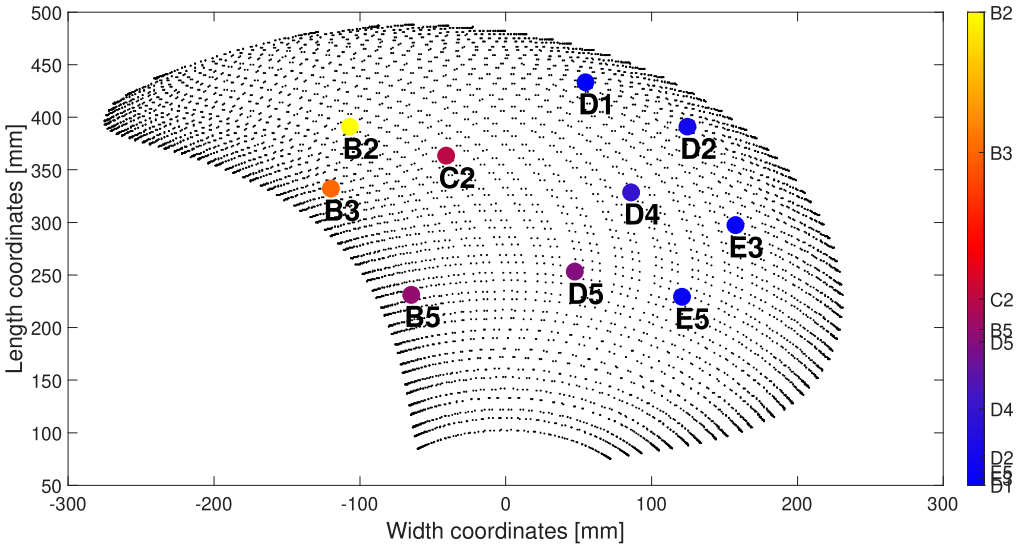

Figure C.6: Mode shape values at embedded piezo-sensors - Mode 3.

C.4. Mode 4 - 579 [Hz]

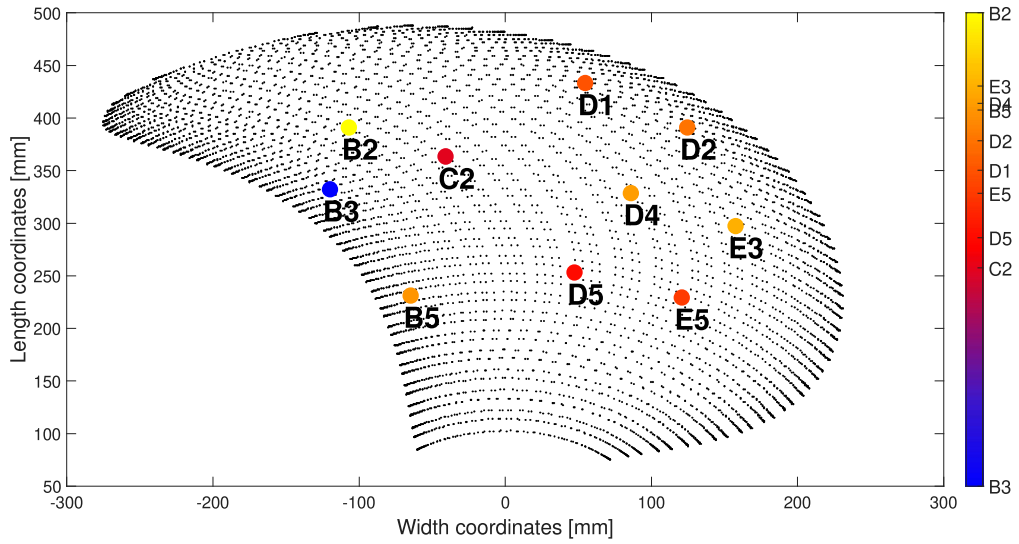

Figure C.7: Mode shape computed by Marc Mentat - Mode 4.

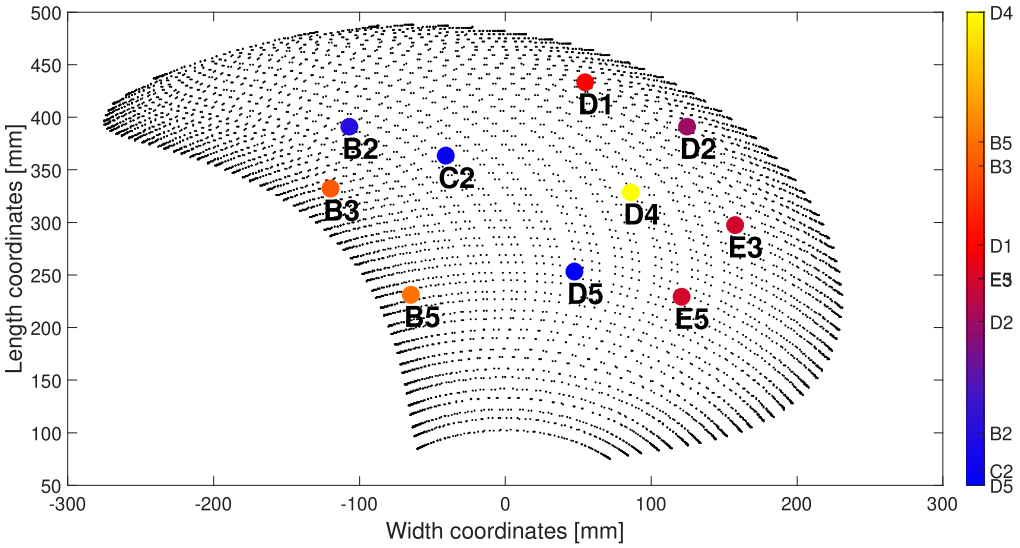

Figure C.8: Mode shape values at embedded piezo-sensors - Mode 4.

C.5. Mode 5 - 701 [Hz]

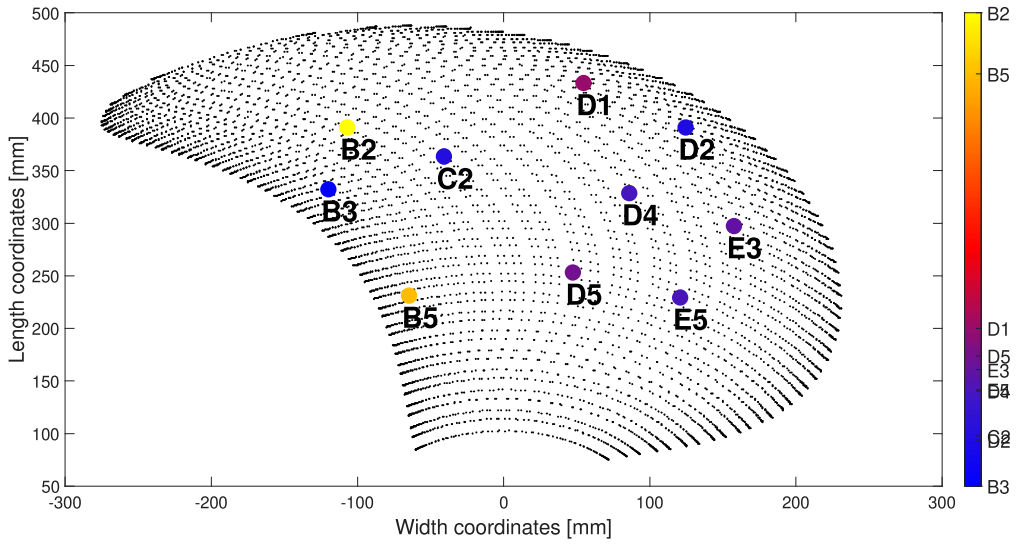

Figure C.9: Mode shape computed by Marc Mentat - Mode 5.

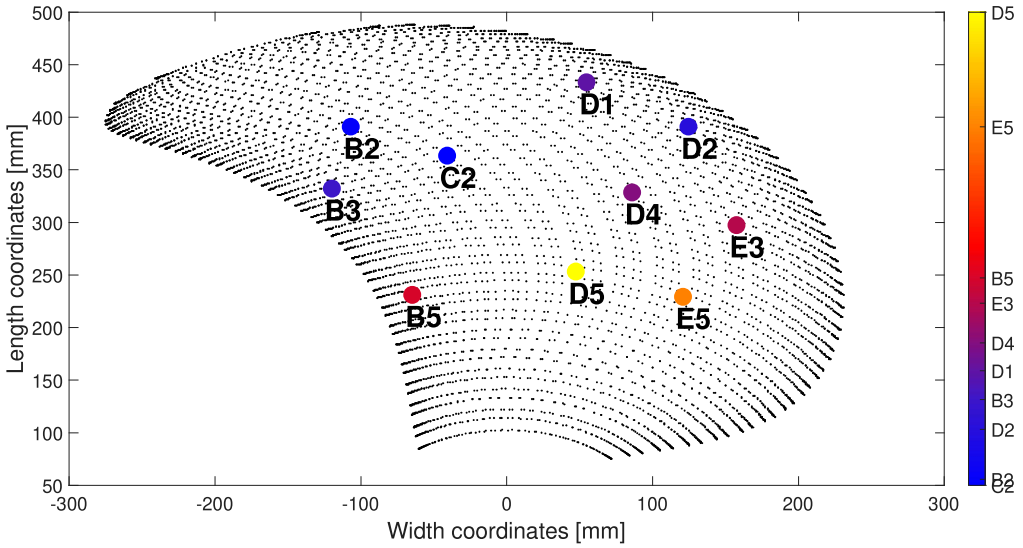

Figure C.10: Mode shape values at embedded piezo-sensors - Mode 5.

C.6. Mode 6 - 818 [Hz]

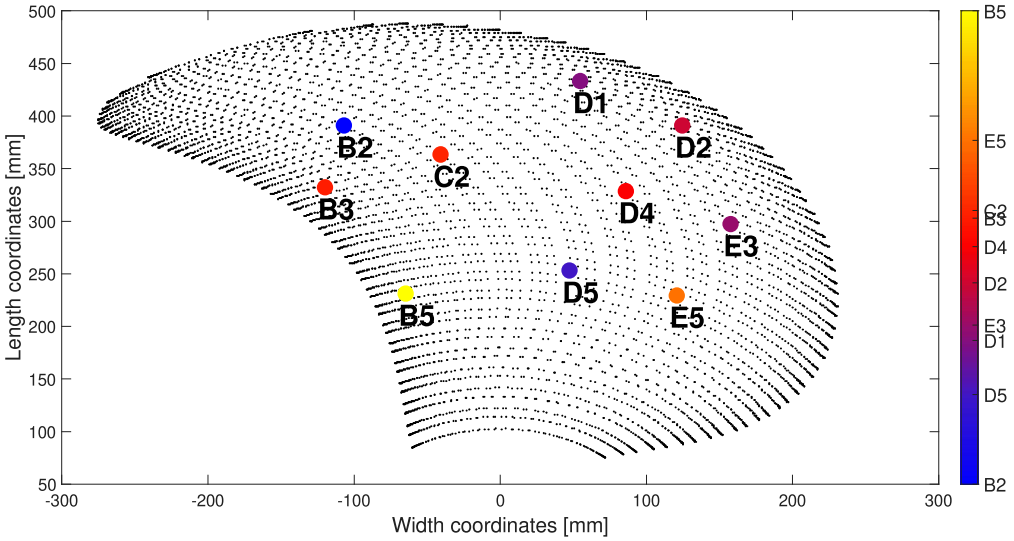

Figure C.11: Mode shape computed by Marc Mentat - Mode 6.

D

Modal Strain Values - FEM & Strain Gauges

D.1. Mode 1

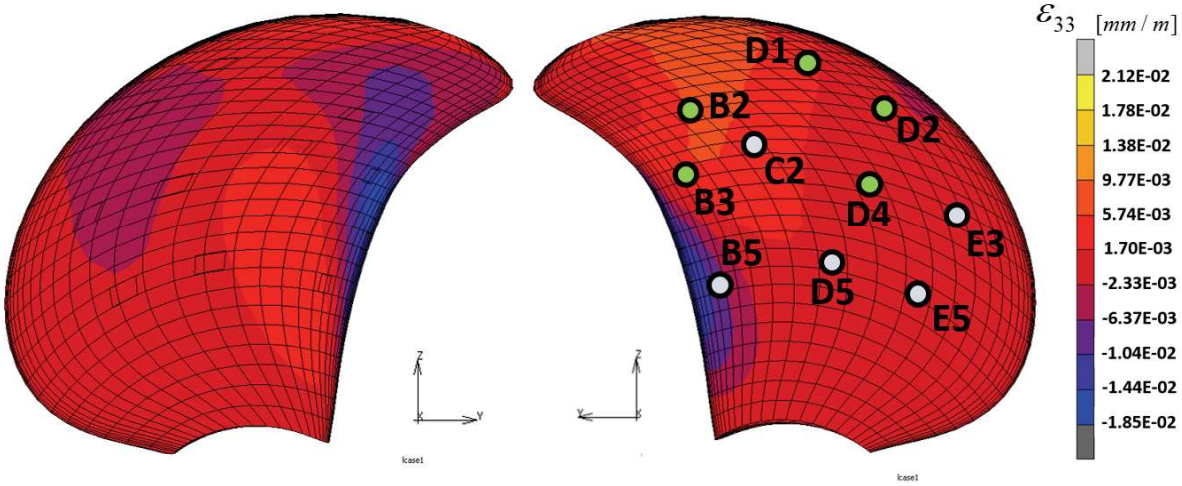

Figure D.1: Strain in z-direction for mode shape 1 computed by Marc Mentat - pressure & suction side.

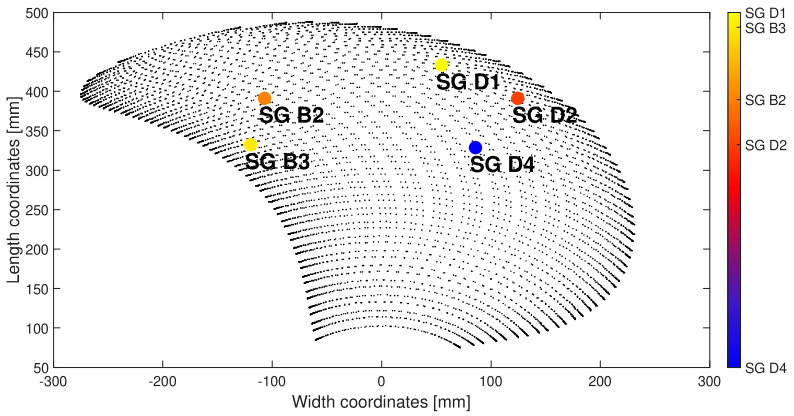

Sensor	Norm. [-]
D1	-0.38
B3	-0.41
B2	-0.53
D2	-0.61
D4	-1

Table D.1: Strain in z-direction for mode shape 1 measured by strain gauges - pressure & suction side.

D.2. Mode 2

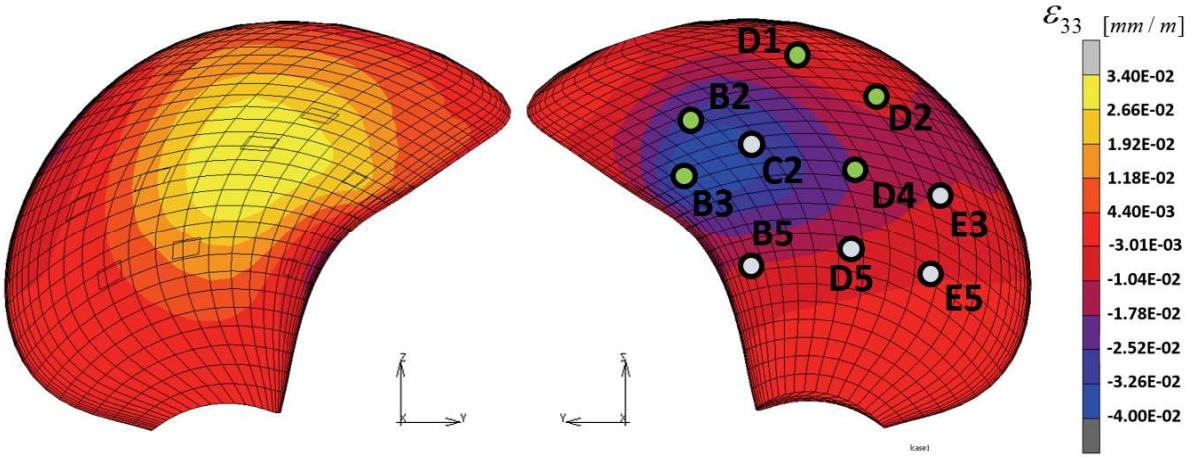

Figure D.2: Strain in z-direction for mode shape 2 computed by Marc Mentat - pressure & suction side.

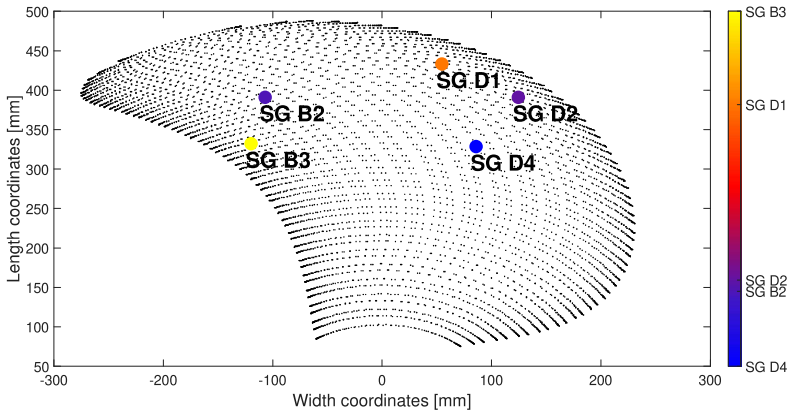

Sensor	Norm. [-]
B3	-0.18
D1	-0.39
D2	-0.80
B2	-0.83
D4	-1

Table D.2: Strain in z-direction for mode shape 2 measured by strain gauges - pressure & suction side.

D.3. Mode 3

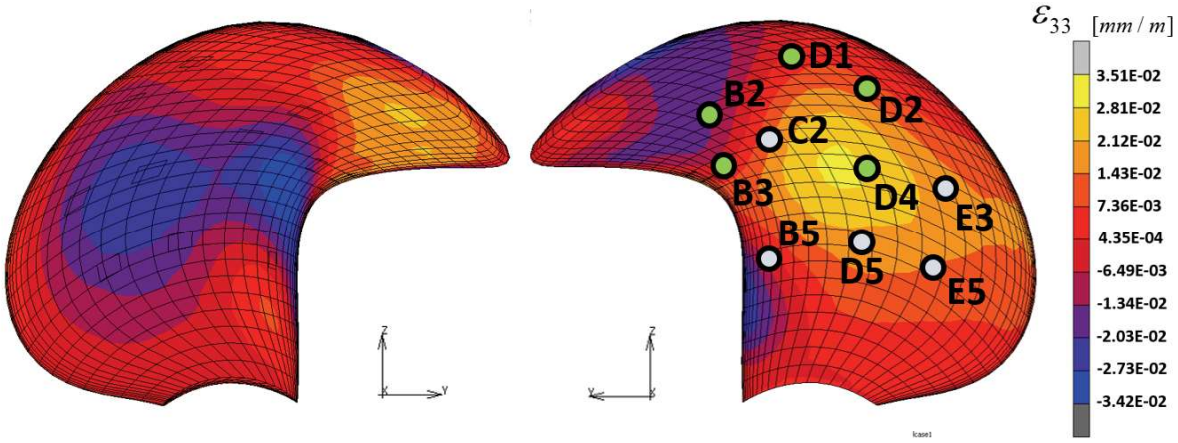

Figure D.3: Strain in z-direction for mode shape 3 computed by Marc Mentat - pressure & suction side.

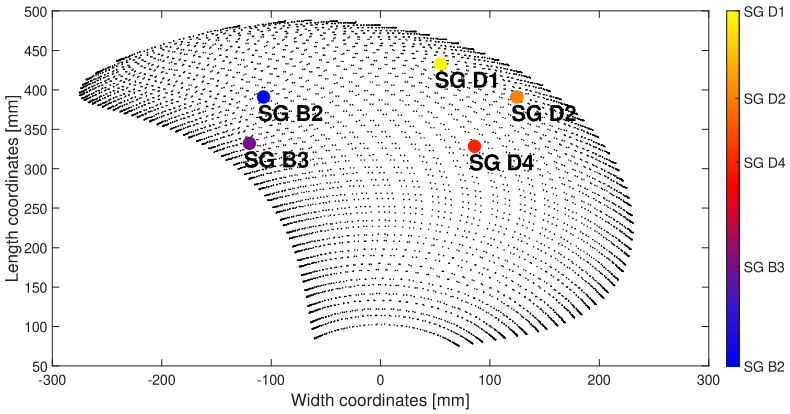

Sensor	Norm. [-]
D1	0.11
D2	-0.16
D4	-0.36
B3	-0.69
B2	-1

Table D.3: Strain in z-direction for mode shape 3 measured by strain gauges - pressure & suction side.

D.4. Mode 4

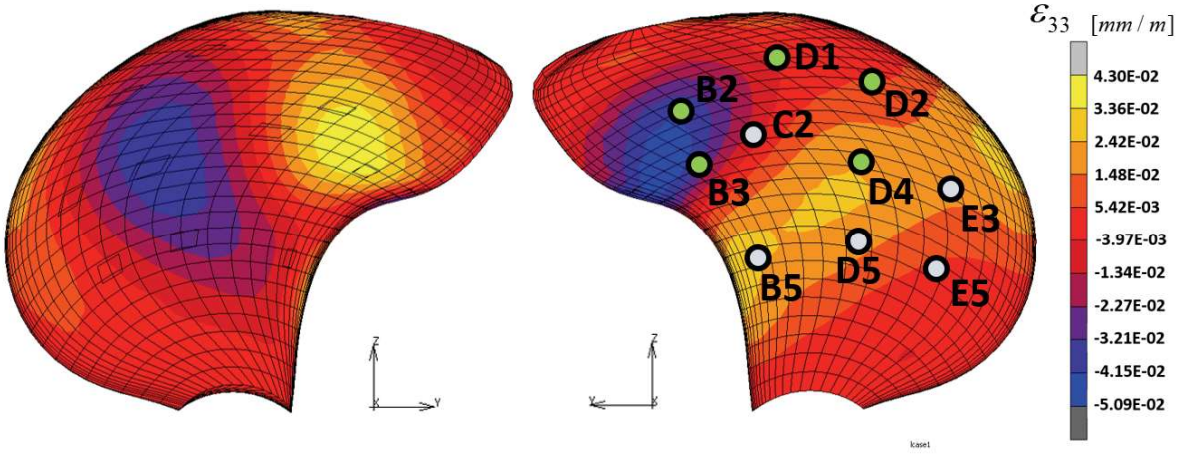

Figure D.4: Strain in z-direction for mode shape 4 computed by Marc Mentat - pressure & suction side.

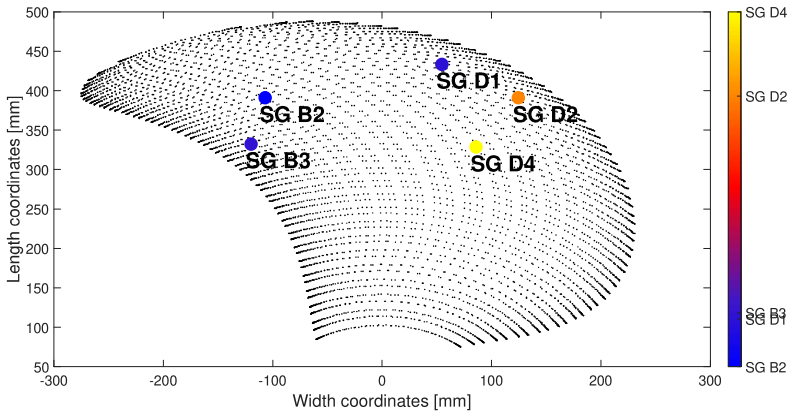

Sensor	Norm. [-]
D4	0.52
D2	0.16
B3	-0.77
D1	-0.80
B2	-1

Table D.4: Strain in z-direction for mode shape 4 measured by strain gauges - pressure & suction side.

D.5. Mode 5

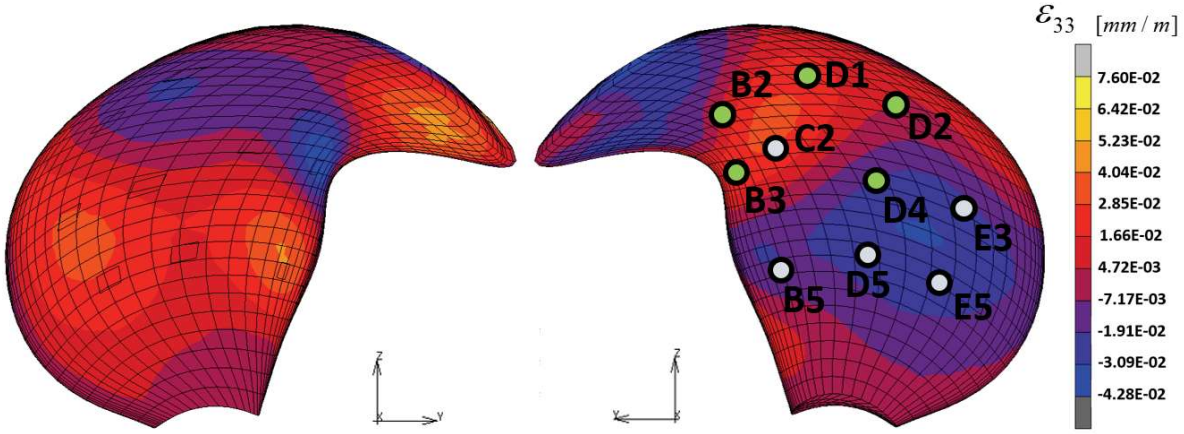

Figure D.5: Strain in z-direction for mode shape 5 computed by Marc Mentat - pressure & suction side.

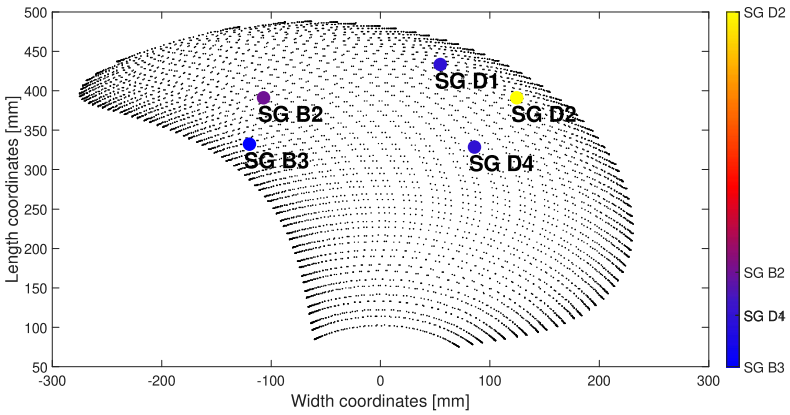

Sensor	Norm. [-]
D2	1
B2	0.59
D4	0.52
D1	0.52
B3	0.43

Table D.5: Strain in z-direction for mode shape 5 measured by strain gauges - pressure & suction side.

D.6. Mode 6

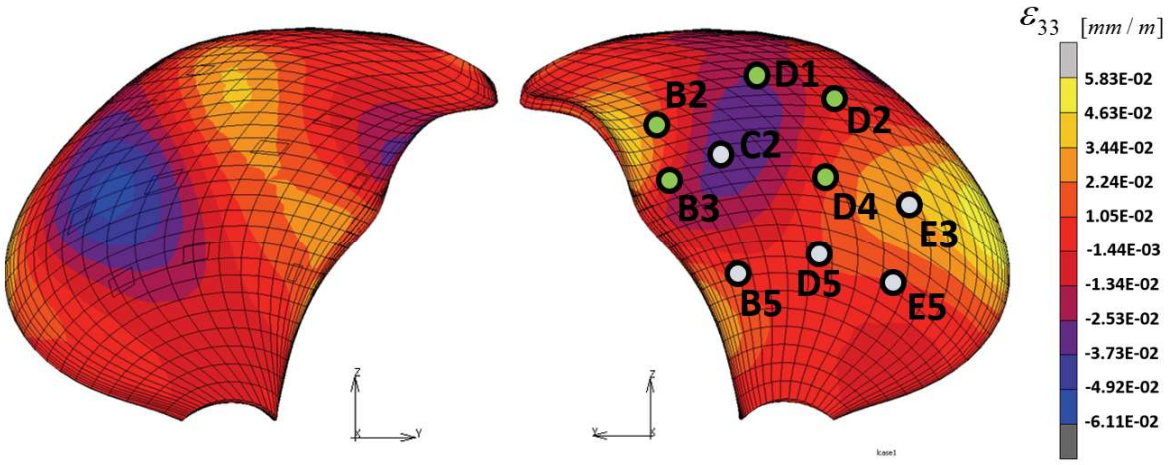

Figure D.6: Strain in z-direction for mode shape 6 computed by Marc Mentat - pressure & suction side.